HHS Public Access

Author manuscript

Dev Cell. Author manuscript; available in PMC 2023 August 08.

Published in final edited form as:

Dev Cell. 2022 August 08; 57(15): 1866–1882.e10. doi:10.1016/j.devcel.2022.06.017.

FoxA1 and FoxA2 control growth and cellular identity in NKX2-1-positive lung adenocarcinoma

Grace Orstad[1,2], **Gabriela Fort**[1,2], **Timothy J Parnell**[1], **Alex Jones**[1,3], **Chris Stubben**[1], **Brian Lohman**[1], **Katherine L. Gillis**[1,2], **Walter Orellana**[1,2], **Rushmeen Tariq**[1], **Olaf Klingbeil**[4], **Klaus Kaestner**[5], **Christopher R. Vakoc**[4], **Benjamin T. Spike**[1,2], **Eric L. Snyder**[1,2,3]

[1.]Huntsman Cancer Institute, University of Utah, Salt Lake City, Utah

[2.]Department of Oncological Sciences, University of Utah, Salt Lake City, Utah

[3.]Department of Pathology, University of Utah, Salt Lake City, Utah

[4.]Cold Spring Harbor Laboratory, Cold Spring Harbor, New York

[5.]Department of Genetics, Perelman School of Medicine, University of Pennsylvania, Philadelphia, Pennsylvania

Abstract

Changes in cellular identity (also known as histologic transformation or lineage plasticity) can drive malignant progression and resistance to therapy in many cancers, including lung adenocarcinoma (LUAD). The lineage specifying transcription factors FoxA1 and FoxA2 (FoxA1/2) control identity in NKX2-1/TTF1-negative LUAD. However, their role in NKX2-1-positive LUAD has not been systematically investigated. We find that *Foxa1/2* knockout severely impairs tumorigenesis in KRAS-driven genetically engineered mouse models and human cell lines. Loss of FoxA1/2 leads to the collapse of a dual-identity state, marked by co-expression of pulmonary and gastrointestinal transcriptional programs, which has been implicated in LUAD progression. Mechanistically, FoxA1/2 loss leads to aberrant NKX2-1 activity and genomic localization, which in turn actively inhibits tumorigenesis and drives alternative cellular identity programs associated with non-proliferative states. This work demonstrates that FoxA1/2 expression is a lineage-specific vulnerability in NKX2-1-positive LUAD and identifies mechanisms of response and resistance to targeting FoxA1/2 in this disease.

Graphical Abstract

Lead Contact: eric.snyder@hci.utah.edu.

Author contributions: GO and ELS designed experiments. GO, GF, AJ, KG, WO, and RT performed experiments. GO, GF, CS, BL, TP, BTS, and ELS analyzed data. ELS performed histopathologic review. OK, CRV and KK provided essential tools and reagents. GO, GF, and ELS wrote the manuscript. All authors discussed results, reviewed and revised the manuscript.

Declaration of Interests: CRV has received consulting fees from Flare Therapeutics, Roivant Sciences, and C4 Therapeutics, has served on the scientific advisory board of KSQ Therapeutics, Syros Pharmaceuticals, and Treeline Biosciences, has received research funding from Boehringer-Ingelheim and Treeline Biosciences, and owns a stock option from Treeline Biosciences.

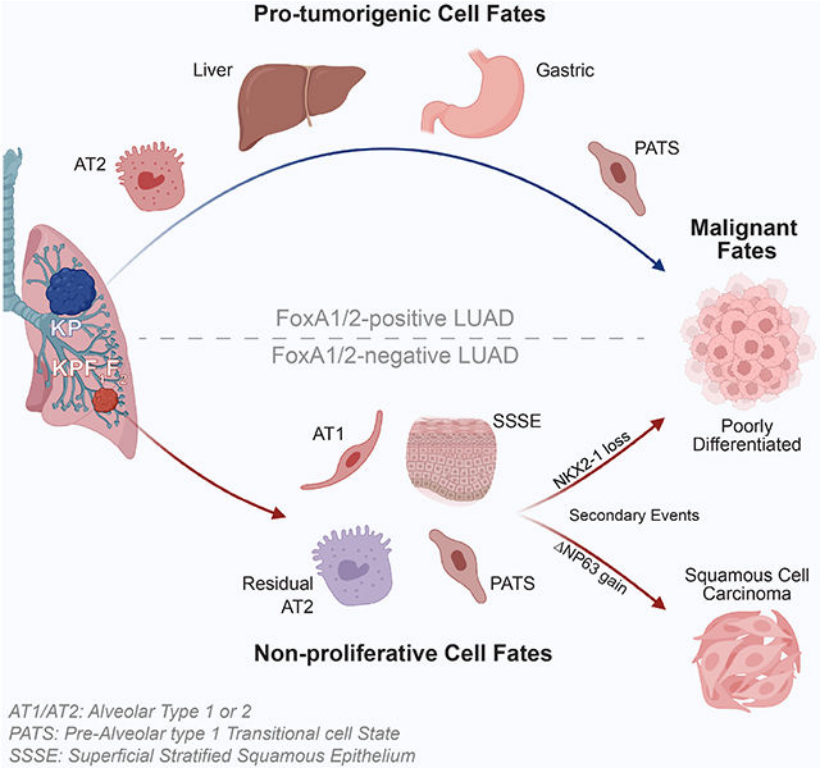

Keywords

FoxA1; FoxA2; NKX2-1; lung adenocarcinoma; cellular identity

INTRODUCTION

The behavior of a cancer cell is initially constrained by the epigenetic state of its cell of origin. Change in cancer cell identity (known as lineage switching/plasticity or histologic transformation) is well characterized as a mechanism of cancer progression and therapeutic resistance (Boumahdi and de Sauvage, 2020; Le Magnen et al., 2018; Quintanal-Villalonga et al., 2020). Lung cancer is the leading cause of cancer death worldwide and lung adenocarcinoma (LUAD), the most frequently diagnosed subtype, exhibits significant heterogeneity in cell identity and differentiation state (Meza et al., 2015; Travis et al., 2011); these characteristics correlate with prognosis, response to therapy, and acquisition of drug resistance (Campos-Parra et al., 2014; Niederst et al., 2015; Russell, 2011; Sun and Yang, 2006). Although epigenetic changes have been implicated, the field lacks a comprehensive understanding of factors governing LUAD heterogeneity and how perturbating these networks alters malignant potential (LaFave et al., 2020; Marjanovic et al., 2020; Tavernari et al., 2021).

Previous work has shown that the transcription factors (TFs) FoxA1, FoxA2, and NKX2-1/TTF1 coordinately regulate cellular identity in LUAD (Camolotto et al., 2018; Li et al., 2015; Snyder et al., 2013; Watanabe et al., 2013; Winslow et al., 2011). NKX2-1 controls

normal lung morphogenesis and differentiation (Bingle, 1997; Bohinski et al., 1994; Little et al., 2019; Little et al., 2021; Liu et al., 2002; Yi et al., 2002) as well as LUAD identity (Snyder et al., 2013; Watanabe et al., 2013; Winslow et al., 2011). NKX2-1 activity is dependent on differential TF interactions in a gene-specific manner, including FoxA1 and FoxA2 (FoxA1/2) in both normal and malignant lung tissue; FoxA1/2 interactions with NKX2-1 enhance the expression of genes with promoters harboring both NKX and FoxA binding motifs (Minoo et al., 2007). FoxA1/2 are closely related paralogs and share roles in establishing and maintaining differentiation of endodermal-derived tissues (Kaestner, 2010). In the lung, FoxA1/2 and NKX2-1 are co-expressed in the trachea, bronchioles, and Type 2 Alveolar (AT2) cells (Besnard et al., 2004; Paranjapye et al., 2020).

FoxA1/2 play context-specific roles in multiple cancers (Gao et al., 2020). For example, *FOXA1* is an oncogene in breast and prostate cancer due to genomic amplifications and point mutations within the forkhead box DNA binding domain (Bernardo and Keri, 2012; Robinson et al., 2013; Teng et al., 2021). In a p53-proficient LUAD genetically engineered mouse model (GEMM), NKX2-1 regulates FoxA1/2 function by dictating whether they bind their pulmonary or gastric targets (Snyder et al., 2013). In the absence of NKX2-1, FoxA1/2 relocalization drives a pulmonary-to-gastric lineage switch; NKX2-1-KO murine tumors closely resemble invasive mucinous adenocarcinoma (IMA), a subtype of human LUAD which also exhibits gastric differentiation (Cha and Shim, 2017). In contrast, in both human and murine NKX2-1+ LUAD, FoxA1/2 bind to regulatory elements of pulmonary target genes (Boggaram, 2009; Snyder et al., 2013; Watanabe et al., 2013). FoxA1/2 and NKX2-1 exhibit extensive co-localization in LUAD, suggesting they may have cooperative functions in cancer mirroring their functions in normal tissue. In a screen of nuclear receptors and their regulators, FOXA1 was identified as pro-tumorigenic in a subset of human LUAD cell lines (Hight et al., 2020).

Despite these observations, FoxA1/2 have not been systematically characterized in NKX2-1+ LUAD, which comprises 75% of human LUAD cases (Bejarano et al., 1996). Here we use GEMMs, organoid cultures, and human cell lines to demonstrate that FoxA1/2 are critical regulators of growth and cellular identity in NKX2-1+LUAD.

RESULTS

FoxA1/2 are required for LUAD growth

We first evaluated expression of NKX2-1 and FoxA1/2 in primary human LUAD via immunohistochemistry (IHC; n=132 tumors). All NKX2-1+ tumors (n=87) express FoxA1 and/or FoxA2. In contrast, 17% (8/45) of NKX2-1–tumors have no detectable FoxA1 or FoxA2 expression (Fig S1A-B, $p<0.0001$, Fisher's Exact test). These data suggest a selective pressure for NKX2-1+ LUAD tumors to retain FoxA1/2.

To investigate the role of FoxA1/2 in NKX2-1+ LUAD, we developed a sequential recombination GEMM to delete *Foxa1* and/or *Foxa2* in KRAS driven, NKX2-1+ lung tumors in vivo. We generated $Kras^{FSF\text{-}G12D/+}$; $Trp53^{Frt/Frt}$; $Rosa26^{FSF\text{-}CreERT2}$; $Foxa1^{F/F}$; $Foxa2^{F/F}$ mice, as well as control mice harboring conditional alleles of either *Foxa1* (Gao et al., 2008) or *Foxa2* (Sund et al., 2000) alone. Delivery of FlpO recombinase to the lung

activates oncogenic *Kras*^{G12D} (Young et al., 2011), inactivates the tumor suppressor *Trp53* (Lee et al., 2012), and induces Cre^{ERT2} at the *Rosa26* locus (Schonhuber et al., 2014). Upon tamoxifen treatment, Cre^{ERT2} deletes *Foxa1* and/or *Foxa2* (KPF$_1$, KPF$_2$, or KPF$_1$F$_2$) specifically in LUAD cells (Fig S1C-D). We first used this model to determine the effect of *Foxa1/2* knockout (KO) at an early timepoint in tumor development (6 weeks post tumor initiation; Fig 1A). Heterozygous KO of a single copy of *Foxa1* and *Foxa2* (KPF$_1^{F/+}$F$_2^{E/+}$; shortened to KP hereafter), as well as homozygous KO of either paralog alone had no effect on proliferation or overall tumor burden two weeks post KO. Simultaneous KO of both *Foxa1* and *Foxa2* caused a significant decrease in both proliferation (7.8-fold) and tumor burden (Fig 1B-C), demonstrating that low-grade LUAD tumors are dependent on FoxA1/2. There was no apparent increase apoptosis at this timepoint (Fig S1E). We next wanted to discern whether *Foxa1/2* KO slowed growth or caused tumor regression. Weekly μCT scans of tumor bearing mice showed that tamoxifen treatment caused an initial decrease in tumor burden followed by disease stasis while vehicle treated mice had a continual increase in tumor burden (Fig S1F).

To evaluate long term consequences of *Foxa1/2* KO, we performed a survival study in which tumors developed to a higher grade prior to tamoxifen or vehicle injections (10 weeks). *Foxa1/2* KO caused a substantial increase in survival, extending median lifespan by 13.5 weeks (Fig 1D). In contrast, heterozygous KO of *Foxa1* and *Foxa2* (Fig 1E), or *Foxa2* KO alone had no impact, and *Foxa1* KO alone lead to a slight increase in median lifespan (1.5 weeks; Fig S1G-H). *Foxa1/2* KO also increased survival in a *BRAF*$^{FSF\text{-}V600E/+}$*; Trp53*$^{Frt/Frt}$ LUAD model (Shai et al., 2015), showing that FoxA1/2 are required for the growth of LUAD with distinct driver mutations (Fig S1I-J). Histological analysis of survival studies is in Table S1.

We derived cell lines from KPF$_1$F$_2$ tumors under either standard 2D or 3D Matrigel-based organoid culture conditions. Treatment with 4-hydroxytamoxifen (4-OHT) generates isogenic pairs that differ solely in the presence or absence of FoxA1/2 (Fig 2A, S2A). In vitro *Foxa1/2* KO significantly decreases proliferation (Fig 2B-C). There is a transient increase in apoptosis 72 hours after 4-OHT treatment, but we did not observe any long-term apoptosis induction (Figure S2D). In subcutaneous tumors, *Foxa1/2* KO caused modest but significant tumor regression followed by slower growth, a pattern which closely matches in vivo μCT analysis (Figure 2D). We identified two distinct morphologies in FoxA1/2-KO subcutaneous tumors: a moderate to poorly differentiated adenocarcinoma (akin to controls) and a distinct sarcomatoid/quasi-mesenchymal component, which exhibited moderately lower NKX2-1 levels (Fig S2B-C).

We next examined FOXA1/2 dependence in NKX2-1+ human LUAD cell lines by knocking out *FOXA1/2* via CRISPR/Cas9. We selected three cell lines harboring *KRAS* mutations that express NKX2-1, as well as one or both of the FoxA1/2 proteins: NCI-H358, NCI-H441, and NCI-H2009. We also targeted *FOXA1/2* in NCI-H1651, an NKX2-1+ LUAD cell line that co-expresses pulmonary and gastric markers. In all four cell lines, *FOXA1/2* KO inhibited proliferation (Fig 2E-F). Combined, these murine and human results demonstrate that FoxA1/2 are required for the growth of NKX2-1+ LUAD.

FoxA1/2 enforce GI-related and AT2 programs

We next sought to determine whether FoxA1/2 regulate cellular identity programs associated with malignant progression in NKX2-1+ LUAD. Recent single cell analyses of the KP LUAD GEMM defined multiple transcriptional programs (TPs) associated with distinct cellular identities that emerge as tumors progress (LaFave et al., 2020; Marjanovic et al., 2020; Yang et al., 2021). Early low-grade tumor cells resemble normal AT2 cells, highly expressing *Nkx2-1* and its canonical AT2 targets. As tumors progress, subsets of LUAD cells activate distinct gastrointestinal (GI) TPs despite the continued expression of *Nkx2-1*. For simplicity, we use the term "dual-identity" to refer to cells in which the AT2 program is simultaneously expressed with GI programs. In late stage disease, some cells reach a terminal poorly differentiated/EMT-like state that lacks both AT2 and GI identities. Transition through dual-identity states is a key component of LUAD evolution, but the mechanisms driving these lineage changes are not fully defined.

To determine which identities are regulated by FoxA1/2 in NKX2-1+ LUAD, we performed scRNAseq on in vivo KPF_1F_2 and KP tumors from mice treated with tamoxifen at 10 weeks and collected at 12 weeks. Using uniform manifold approximation and projection (UMAP) we identified 25 clusters between both genotypes (Fig S3A). Ten of these clusters were identified as tumor cells based on expression of FlpO-induced Cre^{ERT2} transcripts and low levels of stromal specific marker genes (Fig S3B; Table S2). The remaining 15 clusters contain immune cells, endothelial cells, fibroblasts, and normal lung epithelium (Fig S3C, S5A; Table S2). Analysis of only the tumor cell population yielded 13 major clusters (Fig 3A), of which six are KP specific (C1, C3, C4, C5, C6, and C12) and four are KPF_1F_2 specific (C2, C7, C8, and C9). Three clusters contain cells from both genotypes, but cells from KPF_1F_2 samples within these clusters are *Foxa1/2*-positive incomplete recombinants based on equivalent levels of the *Foxa1* exon flanked by loxP sites in both KP and KPF_1F_2 cells (C0, C10, and C11; Fig 3B-C, S3D-E). In contrast, cells in KPF_1F_2 specific clusters are complete recombinants with much lower levels of Exon 2 compared to KP specific clusters (Fig S3F). We also performed bulk RNAseq on isogenic KPF_1F_2 organoid pairs. We identified 1,692 differentially expressed genes: 918 in FoxA1/2+ organoids and 774 in FoxA1/2-KO organoids (padj<0.05, log2FC>|0.585|, Table S3).

Across KP clusters we identified cells expressing the entire continuum of identities that arise throughout LUAD evolution (Marjanovic et al., 2020)(Fig 3D-E, S3F). C0 expresses the AT2-like TP present in cells at an early timepoint in tumor evolution (*Lamp3* and *Nkx2-1*). C10 expresses the mixed AT1/AT2-like TP (*Hopx*). C3, C4, C5, and C6 retain expression of *Nkx2-1* and the AT2-like TP, but also gain expression of the Liver-like and Gastric-like TPs (*Hnf4a* and *Gkn2*); these clusters contain cells with the dual-identity state that emerges as KP LUAD tumors evolve. C1 cells express both Gastric-like and GI epithelium-like TPs, as well as the "Highly Mixed" TP associated with the high-plasticity cell state described by (Marjanovic et al., 2020) (*Cldn4*). Finally, in C12 we isolated a subset of cells that express the terminal, highly aggressive EMT TP that is found only in advanced, high grade LUAD (*Hmga2*). As expected, cells in the G2/M phase cluster separately from other tumor cell populations (C11).

Because KP tumors contain the entire spectrum of cellular identities that emerge throughout LUAD progression in this model, we can examine differences between the KP and KPF_1F_2 clusters to determine which LUAD differentiation states are dependent on FoxA1/2. We found that FoxA1/2-KO cells still express markers of the AT1/AT2 (*Hopx* in C2, C8, and C9) and Highly Mixed TPs (*Cldn4* in C2, C7 and C9; Fig 3D-F). However, FoxA1/2 are required for full activation of the AT2-like and Gastric/Liver-like fates.

Our most striking observation is that the dual-identity, simultaneously pulmonary and gastric cellular state is completely dependent on FoxA1/2. Liver-like and Gastric-like TPs are absent in FoxA1/2-KO clusters (*Hnf4a* and *Gkn2*; Fig 3D-E, S3F,H). Nearly 100% of the cells with high expression of these programs come from KP-specific clusters (Fig 3F). Loss of gastric identity is consistent at the protein level in tumors and organoids; a subset of FoxA1-2+ cells are positive for both NKX2-1 and HNF4α, but FoxA1/2-KO cells completely lack HNF4α (Fig 3G, S3G). In addition, HNF4α levels decrease following *FOXA1/2* KO in the dual-identity human LUAD cell line H1651 (Fig S3I). In vitro we see an overall enrichment for the Gastric, GI epithelium, and Liver TPs in FoxA1/2+ organoids, and canonical gastric and endodermal markers are significantly decreased following *Foxa1/2* KO (Fig 3H-I). These data show that FoxA1/2 are essential drivers of the gastric/endodermal states that are a critical phase of LUAD evolution.

FoxA1/2 are also important drivers of AT2-like cellular identity, albeit to a lesser extent than the Gastric and Liver identities. The AT2-like program is very low in KPF_1F_2 C7, and is expressed in C2, C8 and C9 at a lower level than the KP AT2-like C0 (*Lamp3* and *Nkx2-1*; Fig 3D-E, S3F). At the individual gene level, we find that the decline in AT2 identity following *Foxa1/2* KO is a consequence of a partial downregulation of AT2 genes in C2, C8 and C9 when compared to the AT2-like C0 (Fig S3H,J). Moreover, there are specific AT2 genes in each cluster (such as *Napsa* in C2 and C8) that are expressed at approximately the same level as C0 (Fig S3H). Consistent with these observations, we see a decrease, but not complete loss, of AT2 markers SPB and SPC by IHC after *Foxa1/2* KO (Fig 3J). In vitro, we also see an overall enrichment of the AT2 TP in FoxA1/2+ organoids (Fig 3H). However, while some individual AT2 markers are significantly decreased following *Foxa1/2* KO (*Cxcl15, Lamp3, Lyz2, Sftpa1* and *Sftpc*), others are only slightly decreased (*Sftpb*) or virtually unchanged (*Napsa*; Fig 3K). Expression of AT2 markers *SFTPA1* and *SFTPB* also decreases following *FOXA1/2* KO in human LUAD cell line H441 (Fig S3K). These data show that FoxA1/2 are needed for maximal expression of the AT2-like TP, but other pulmonary transcription factors may act independently of FoxA1/2 to activate some elements of AT2 identity. In sum, we find that FoxA1/2 are critical drivers of the dual-identity state that emerges as LUAD tumors evolve. Upon *Foxa1/2* KO, tumors decrease their expression of an AT2-like identity and completely lose gastric and endodermal TPs (Fig 3L).

FoxA1/2 suppress alternative pulmonary and stratified squamous transcriptional programs

We next sought to understand the transcriptional state(s) to which LUAD cells equilibrate in the absence of FoxA1/2. We first evaluated relative levels of TPs associated with normal lung tissue using gene signatures of normal AT1 and AT2 cells (Travaglini et al., 2020).

We found that the Travaglini AT2 signature is detectable in FoxA1/2-KO C2, C8, and C9 (Fig 4A), but at a lower level than C0 FoxA1/2+ cells, consistent with our analysis of the Marjanovic AT2-like LUAD signature (Fig 3D-E, S3J). The Travaglini AT1 signature is readily detectable in FoxA1/2-KO C2 and C7 (Fig 4B), as are an AT1 signature from the LungGENS database (Du et al., 2015) (Fig S4A) and AT1 genes uniquely dependent on NKX2-1 as defined by (Little et al., 2019) (Fig 4C). Close inspection of C2 reveals an inverse correlation between AT2 and AT1 identities within this cluster (Fig S4B-C). FoxA1/2-mediated inhibition of AT1 differentiation is also evident in organoids. Using Gene Set Enrichment Analysis (GSEA), we found that *Foxa1/2* KO in organoids impairs AT2 differentiation and promotes AT1 differentiation (Fig 3H, 4D). At the protein level, a higher proportion of LUAD tumor cells are positive for the AT1 marker HOPX following *Foxa1/2* KO (Fig 4E). Together these data suggest that loss of FoxA1/2 promotes an AT1 cellular state.

The 'Highly Mixed'/*Cldn4*-high program from (Marjanovic et al., 2020) is found in both FoxA1/2+ and FoxA1/2-KO clusters (C1 vs. C7, Fig 3D-F). Interestingly, three recent publications describe a distinct *Cldn4*-high alveolar cell state that emerges as AT2 cells differentiate into AT1 cells in response to lung injury, termed Pre-Alveolar type-1 Transitional cell State (Kobayashi et al., 2020) (PATS; also described by (Strunz et al., 2020) as Alveolar Differentiation Intermediate; ADI, and (Choi et al., 2020) as Damage-Associated Transient Progenitors; DATPs). This is a unique transitional cell population that emerges in response to injury and is marked by high *Cldn4* levels and activation of NFκB and TGFβ signaling. The PATS/ADI TPs are expressed in a subset of KP and KPF_1F_2 LUAD cells and overlap with the 'Highly Mixed' TP in our dataset (Fig 4F, S4D). We see higher protein levels of PATS/ADI markers CLDN4 and SFN following *Foxa1/2* KO in tumors (Fig 4G-H; gene expression UMAPs 4I). Additionally, GSEA shows enrichment of these TPs upon *Foxa1/2* KO in organoids (Fig 4D). This suggests that the LUAD cells previously described as 'Highly Mixed' may have activated the TP of PATS/ADI transitional cells that emerge in response to lung injury. We note that in scRNA-seq data, levels of both PATS/ADI and AT1 signatures are not necessarily higher in specific FoxA1/2-KO clusters compared to controls, but that a higher fraction of cells express these programs, which likely explains their enrichment in bulk RNA-seq data.

GSEA of organoid RNAseq provided additional insights into the cellular identities adopted by FoxA1/2-KO cells, revealing enrichment of gene sets expressed in the superficial layers of the stratified squamous epithelium (SSSE) in FoxA1/2-KO organoids (Fig 4J-K; Table S5). GSEA of each scRNAseq cluster revealed that a similar array of TPs associated with stratified squamous differentiation were enriched in FoxA1/2-KO C7 (Table S3; Fig 4L). Specific genes highly expressed in FoxA1/2-KO cells in vivo include *Sfn*, a marker of keratinocytes and PATS/ADI cells, *Cnfn*, a marker of the SSSE, and *Cryab*, a reported marker of SSSE and AT1 cells (Fig 4I). At the protein level, the majority of FoxA1/2-KO tumors are positive for SFN (>75%), while most FoxA1/2+ tumors lack any SFN (Fig 4H; positive staining in normal SSSE Fig S4E). Alpha crystallin-β chain (the *Cryab* gene product), is detected in a subset of FoxA1/2-KO tumor cells, but not controls. Of note, in our analysis this protein was detectable in normal SSSE but not AT1 cells (Fig S4F). Despite induction of many SSSE genes, ΔNp63 (a master regulator of squamous differentiation and

an oncogene in squamous cell carcinoma (SCC)) is undetectable in FoxA1/2 KO tumor cells (Fig S4G)(Moses et al., 2019). Thus, *Foxa1/2* KO causes an incomplete shift toward a squamous differentiation program in a subset of LUAD cells, but the absence of ΔNp63 may prevent full SCC transdifferentiation.

We next wanted to assess whether these identity patterns exist in human disease, so we analyzed *NKX2-1*-high LUAD samples from TCGA's PanCancer Atlas (n=402/516) and grouped patients into *FOXA1/2*-high and *FOXA1/2*-low cohorts (n=114 and 23, respectively). We identified DEGs between these cohorts and assessed enrichment of relevant TPs via GSEA (Table S3). In support of our in vivo and in vitro murine RNAseq data, we find that AT2 and Gastric identities are significantly enriched in *FOXA1/2*-high tumors. In contrast, *FOXA1/2*-low tumors exhibit a significant enrichment of AT1, PATS/ADI, and Keratinocyte differentiation states (Fig 4M). Altogether, these data show that FoxA1/2 inhibit alternative alveolar and stratified squamous differentiation states in NKX2-1+ LUAD. Specifically, *Foxa1/2* KO causes a partial loss of AT2-like identity, with a concomitant increase in the percentage of cells expressing markers of alternative alveolar cell types, such as AT1 or PATS. Moreover, a subset of LUAD cells activate TPs associated with the SSSE after *Foxa1/2* KO.

Deletion of both *Foxa1* and *Foxa2* is required for cellular identity transitions

In order to understand the individual contributions of FoxA1 and FoxA2 to the cell fate phenotypes described in Figures 3 and 4, we performed RNAseq on isogenic pairs of KPF_1 and KPF_2 organoids (n=3 and 2 independent organoid lines, respectively). *Foxa1* KO led to 284 DEGs: 244 in FoxA1+ organoids and 40 in FoxA1-KO organoids. *Foxa2* KO yields 760 DEGs: 435 in FoxA2+ organoids and 325 in FoxA2-KO organoids. In contrast, simultaneous *Foxa1* and *Foxa2* KO led to 1692 DEGs (padj<0.05 and log2FC>|0.585|).

We then intersected DEGs from each genotype and found that 75% of gene expression changes (1269/1692) observed in KPF_1F_2 isogenic organoid pairs are unique to this genotype (Fig S4H). Thus, the large majority of observed transcriptional changes require loss of both FoxA1 and FoxA2. In addition to yielding fewer DEGs overall, single KO of either *Foxa1* or *Foxa2* results in gene expression changes that are significantly lower in magnitude than KO of both (Fig S4I). These data reveal that FoxA1 plays a smaller role in transcription than FoxA2, but loss of both paralogs is required for maximal transcriptional changes.

Although there are substantially fewer DEGs following individual *Foxa1* or *Foxa2* KO, we proceeded to investigate the individual contribution of each paralog in regulating cell fate. Overall, KO of either *Foxa1* or *Foxa2* alone does not inhibit gastric or AT2 identities at the RNA or protein level (Fig S4J-L). Additionally, individual KO does not result in induction of SSSE TPs (Fig S4J). Together, these data illustrate the functional redundancy of FoxA1 and FoxA2; loss of both TFs is required to observe changes in tumor growth (Fig 1B-E, S1G-H) and differentiation state.

FoxA1/2 loss alters resident macrophage and neutrophil populations in the TME

To determine whether *Foxa 1/2* KO in tumor cells has an effect on the tumor microenvironment (TME), we profiled each non-tumor cell population in our scRNAseq (Fig S3A-C, S5A). We identified significant transcriptional differences within two immune cell compartments: myeloid cells and neutrophils. Analysis of the myeloid clusters revealed multiple transcriptionally defined clusters corresponding to four established cell types based on expression of canonical marker genes (Fig S5B-E, Table S2) (Casanova-Acebes et al., 2021; Maier et al., 2020). Most myeloid clusters overlapped between genotypes, but we identified two distinct clusters of alveolar macrophages that were largely unique to either KPF_1F_2 tumors (C1) or KP tumors (C0). Interestingly, the top DEG between these two clusters was *Il1b*, a pro-inflammatory cytokine that marks tumor suppressive M1-like macrophages, in addition to enrichment of several other M1-associated genes (Fig S5E,G; Table S4). GSEA of C1 vs C0 DEGs revealed pro-inflammatory TNFα signaling as the top statistically enriched pathway in C1 (Fig S5F). Together, these results indicate that alveolar macrophages in KPF_1F_2 tumors adopt a pro-inflammatory profile, which could contribute to slower tumor growth. Intriguingly, IL-1β secreted from macrophages also promotes the PATS/DATP intermediate cell state in alveolar regeneration models (Choi et al., 2020). Thus, KPF_1F_2 TME macrophages may activate or reinforce a PATS fate in FoxA1/2 KO tumors.

We also noted an enrichment in the neutrophil recruitment chemokines *Cxcl1* and *Cxcl2* in C1 relative to C0 (Fig S5G). Because *Nkx2-1* KO accelerates transdifferentiation from LUAD to lung squamous cell carcinoma by enhancing neutrophil recruitment to the TME (Mollaoglu et al., 2018), and AT2 identity is also partially lost upon *Foxa1/2* KO in the present study, we hypothesized that in the KPF_1F_2 model both macrophages and tumor cells may coordinately recruit neutrophils to the TME where they might similarly impact tumor cell state transitions (AT2 to squamous). Indeed, we found that KPF_1F_2 tumor cells also express higher levels of *Cxcl1, Cxcl2*, and *Cxcl5* than KP tumor cells (Fig S5H).

Analysis of the neutrophils revealed cellular subtypes with differences in *Siglecf* expression, a marker of pro-tumor neutrophils in the KP model (Engblom et al., 2017; Zilionis et al., 2019) (Fig S5I-K). $Siglecf^{high}$ neutrophils expressed genes associated with the pro-tumor subtype, while the $Siglecf^{low}$ population expressed higher levels of canonical neutrophil markers (Engblom et al., 2017; Zilionis et al., 2019) (Fig S5L-M). While the $Siglecf^{high}$ population was more evenly distributed between genotypes, the $Siglecf^{low}$ cluster was almost entirely from KPF_1F_2 samples (Fig S5O). Of note, the Cxc chemokine receptor 2 gene (**Cxcr2**) was expressed at higher levels in the KPF_1F_2-specific $Siglecf^{low}$ cluster (Fig S5N). This may indicate recruitment of this potentially functionally distinct $Siglecf^{low}$ neutrophil subset to the TME by *Cxcl1/2/5*-expressing tumor cells and macrophages upon *Foxa1/2* KO in tumor cells (Fig S5N).

Finally, we asked whether the increase in M1 macrophage markers and neutrophil chemoattractants might reflect distinct immune interactions within the TME specifically in KPF_1F_2 tumors. To model intercellular communication between major immune cell subtypes in our scRNAseq dataset, we utilized the CellChat computational package (Jin et al., 2021). CellChat analysis inferred stronger interactions between neutrophils, tumor

cells, and macrophages in KPF_1F_2 than KP tumors (Fig S5P). We predict that increased communication between these cells could reinforce the PATS and SSSE TPs in KPF_1F_2 tumor cells *in vivo*, while *Foxa1/2* KO induces pro-inflammatory programs that hinder LUAD tumor growth. Importantly, we observe induction of these TPs in vitro (Fig 4D, J), suggesting that the TME is not strictly required for acquisition of these fates, but may reinforce them in vivo.

NKX2-1 is responsible for a subset of gene expression changes induced by *Foxa1/2* deletion

NKX2-1 dictates both AT2 and AT1 cell fate by controlling a distinct set of genes in each cell type (Little et al., 2019; Little et al., 2021). We therefore decided to investigate whether changes in NKX2-1 activity might drive changes in pulmonary identity programs caused by *Foxa1/2* KO. We first sought to determine which gene expression changes induced by *Foxa1/2* KO can be attributed to NKX2-1. In order to answer this question, we performed RNAseq on organoid cultures transduced with shNKX2-1 (KD) or shScramble after treatment with 4-OHT or vehicle (Fig 5A). Intersection of DEGs from each conditions reveals that NKX2-1 is required for ~25% of gene expression changes caused by *Foxa1/2* KO (Fig 5B; Table S6). Specifically, 22% of the genes induced by *Foxa1/2* KO and 31% of genes that decline after *Foxa1/2* KO are NKX2-1-dependent (Fig 5C).

We then investigated how NKX2-1 contributes to the activation of the AT1, AT2, and PATS identities. All three alveolar TPs are enriched in the FoxA1/2-KO/NKX2-1+ organoids in comparison to the FoxA1/2-KO/shNKX2-1 organoids. This indicates that overall, NKX2-1 is important for both the maintenance of residual AT2 identity and the activation of the de novo AT1 and PATS TPs after *Foxa1/2* KO (Fig 5D). At the individual gene level, we observed nuanced transcriptional dynamics of key AT2 markers. Expression of canonical AT2 genes, *Sftpc* and *Sftpb*, is regulated by both FoxA1/2 and NKX2-1 in an additive manner; *Foxa1/2* KO and NKX2-1 KD independently decrease the expression of these genes, but a combination of both yields the maximal decrease (Fig 5E). In contrast, *Lamp3* and *Sftpa1* expression is maximally decreased upon *Foxa1/2* KO, and *Nkx2-1* KD inhibits their expression only in FoxA1/2+ cells, but not FoxA1/2-KO cells (Fig 5F). Thus, NKX2-1 can partially activate some, but not all, AT2 marker genes in the absence of FoxA1/2. Conversely, *Napsa* expression exhibits dependence solely on NKX2-1 (Fig 5G). The complex transcriptional hierarchy between these TFs at AT2 marker genes explains why *Foxa1/2* KO decreases, but does not completely ablate, the AT2 signature in LUAD.

We also asked whether NKX2-1 contributes to the activation of the SSSE in the absence of FoxA1/2. We found that SSSE TPs are also enriched in the FoxA1/2-KO/NKX2-1+ organoids when compared to the FoxA1/2-KO/shNKX2-1 organoids, indicating that NKX2-1 is important for full activation of the SSSE phenotype induced by *Foxa1/2* KO (Fig 5D). A subset of SSSE genes are NKX2-1-dependent (e.g. *Krt14* and *Lor*, Fig 5H), whereas others are NKX2-1 independent (e.g. *Krt16* and *Cldn3*, Fig 5I). These data show that NKX2-1 contributes to, but is only partially responsible for, activation of the SSSE identity induced by *Foxa1/2* KO.

FoxA1/2 regulate cell type-specific NKX2-1 binding in LUAD

To understand how NKX2-1 drives unique TPs after *Foxa1/2* KO, we performed ChIPseq for NKX2-1 in FoxA1/2+ and FoxA1/2-KO organoids. We identified a total of 36,958 NKX2-1 peaks via MACS2: 16,911 peaks in FoxA1/2+ organoids and 32,358 peaks in FoxA1/2-KO organoids (Table S7). HOMER transcription factor motif analysis of these peaks showed that NKX binding motifs are enriched in both conditions while FOX motifs are exclusively enriched in FoxA1/2+ NKX2-1 peaks (Fig S6A). Both sets of peaks share similar genomic occupancy profiles (Fig S6B). We also performed ChIPseq for FoxA2 in FoxA1/2+ organoids and identified 6770 individual FoxA2 peaks. HOMER analysis of FoxA2 peaks revealed enrichment for FOX, HNF4, NKX, FOS/JUN, ETS, KLF, and GATA family transcription factor motifs (Fig S6C).

In addition to club cells and AT2 cells, NKX2-1 is also expressed in normal AT1 cells, and differential NKX2-1 activity drives alveolar cell fate (Little et al., 2019; Little et al., 2021). We therefore investigated whether differential NKX2-1 binding drives the shift in alveolar cell identity upon loss of FoxA1/2. (Little et al., 2021) performed NKX2-1 ChIPseq in normal murine AT1 and AT2 cells to identify AT1-specific and AT2-specific NKX2-1 binding sites. In alignment with our gene expression data, there is an overall increase in NKX2-1 localization to its AT1-specific binding sites in the absence of FoxA1/2, whereas global NKX2-1 localization at AT2-specific sites is unchanged (Fig 6A-B). We performed differential analysis on published ATAC-seq data from purified AT1 and AT2 cells (Little et al., 2021) to identify unique vs. shared open chromatin regions. We intersected our FoxA2 peaks with these open chromatin regions, and found that 56% of FoxA2 peaks are found in AT2-specific open chromatin regions while only 4% of peaks are located within AT1-specific open chromatin regions (Fig S6D). Together these data suggest that FoxA1/2 regulate NKX2-1 genomic occupancy, which in turn dictates the alveolar identity adopted by tumor cells.

To investigate the impact of FoxA1/2 loss on NKX2-1 genomic localization in more depth, we used MAnorm2 (Tu et al., 2021) to identify a total of 2,758 high confidence differential NKX2-1 binding sites: 1,262 in FoxA1/2+ cells and 1,496 in FoxA1/2-KO cells (Fig 6C; Table S7). We next intersected differential NKX2-1 peaks with FoxA2 peaks and found striking colocalization between FoxA2 and NKX2-1 in FoxA1/2+ cells; 71% of differential NKX2-1 peaks in FoxA1/2+ cells overlap with FoxA2 peaks while only 5% of NKX2-1 peaks in FoxA1/2-KO cells overlap with FoxA2 peaks from control cells (Fig 6C,F).

HOMER analysis (Table S7) of differential and common peaks (Fig 6D-E, S6E) identified two interesting patterns beyond the expected FOX motif and NKX motif distribution. (1) Differential AT2 TF distribution: CEBP, NFI, and GRHL family TFs all play a role in AT2 differentiation (Bachurski et al., 2003; Herriges et al., 2012; Little et al., 2021; Varma et al., 2012). CEBP motifs are enriched in FoxA1/2+ and static NKX2-1 peaks, while NFI and GRHL motifs are enriched in a FoxA1/2-KO context. This suggests that *Foxa1/2* KO alters the specific AT2-regulating TFs with which NKX2-1 associates. (2) NFκB enrichment in FoxA1/2-KO NKX2-1 ChIP peaks: activation of the NFκB pathway is a hallmark of the PATS/ADI cell population that emerges in response to alveolar injury (Kobayashi et al., 2020; Strunz et al., 2020). The presence of an NFκB motif in FoxA1/2-KO-specific NKX2-1

peaks suggests cooperation between NKX2-1 and NFκB signaling in promoting a PATS-like identity.

We intersected FoxA2 peaks and differential NKX2-1 peaks with DEGs associated with *Foxa1/2* KO. FoxA2 peaks are associated with 12.5% of DEGs. Direct binding by differential NKX2-1 peaks is significantly associated with gene activation rather than repression (Fig 6G). For example, there are two de novo NKX2-1 peaks in FoxA1/2-KO cells within the promoter of AT1 marker Podoplanin (*Pdpn*: Fig 6H). Additionally, two NKX2-1 peaks that co-localize with FoxA2 in the promoter of AT2 marker *Sftpa1* are only present in FoxA1/2+ cells (Fig 6I). Corresponding with the loss of NKX2-1 peaks, *Foxa1/2* KO is sufficient for maximal reduction in *Sftpa1* transcript levels (Fig 5F). In contrast, we find both differential and common NKX2-1 peaks near *Sftpb*, regardless of the presence or absence of an overlapping FoxA2 peak (Fig 6J). This likely explains why NKX2-1 can partially activate *Sftpb* transcription in the absence of FoxA1/2 (Fig 5E). Expression of the AT2 marker *Napsa* is not impacted by *Foxa1/2* KO and does not have a FoxA2 peak, but expression does decrease upon NKX2-1 KD. Correspondingly, NKX2-1 binds *Napsa* independent of FoxA1/2 status (Fig 5G, 6K).

Taken together, these data underscore the complex transcriptional relationship between FoxA1/2 and NKX2-1 in regulation of pulmonary identity. FoxA1/2 regulate alveolar cell type-specific localization of NKX2-1 in LUAD, and de novo NKX2-1 binding upon *Foxa1/2* KO is correlated with the activation of AT1 and AT2 cellular fates.

NKX2-1 impairs tumor growth in the absence of FoxA1/2

We next wanted to determine whether de novo NKX2-1 activity contributes to the growth arrest caused by *Foxa1/2* KO. Stochastic NKX2-1 loss can facilitate progression of KP LUAD (Winslow et al., 2011). We therefore predicted that if NKX2-1 also restrains the growth of FoxA1/2-KO tumors, there would be selection for NKX2-1 loss in FoxA1/2-KO tumors over time. Histological analysis of tamoxifen treated mice in our survival study (Fig 1D) revealed two morphologically distinct classes of tumors that grew to macroscopic size despite the absence of FoxA1/2. The first class, found in 80% of tamoxifen treated KPF_1F_2 mice (n=8/10 mice histologically evaluated), is characterized by a keratinizing SCC morphology (Table S1). These SCCs express squamous lineage specifier ΔNp63 and retain NKX2-1 expression, but at reduced levels compared to adenocarcinomas (Fig S7A). The second class, found in 30% of tamoxifen treated KPF_1F_2 mice, consists of poorly differentiated, high grade tumors that are NKX2-1– (Fig 7A). Because *Foxa1/2* KO does not directly lead to loss of NKX2-1 or gain of ΔNp63 expression (Fig 1A, S4E), these observations point to specific stochastic events that might enable LUAD to overcome *Foxa1/2* KO overtime.

Based on these correlations, we sought to determine whether NKX2-1 loss is sufficient to rescue *Foxa1/2* KO. First, we initiated $Kras^{G12D}$-driven p53-proficient tumors, allowed growth for 6 weeks, and then administered tamoxifen to delete *Foxa1* alone (KF_1), *Foxa1* and *Foxa2* (KF_1F_2), *Nkx2-1* alone (KN), or *Nkx2-1, Foxa1* and *Foxa2* (KNF_1F_2). Tumors progressed for 6 more weeks before tissue was collected. *Nkx2-1* KO rescued the effects of *Foxa1/2* KO on tumor growth, resulting in a comparable tumor burden in KNF_1F_2 and KN

mice (Fig 7B). As expected (Camolotto et al., 2018; Snyder et al., 2013), tumor burden in KN was highest overall. We have previously shown that KNF_1F_2 mice develop two distinct tumor types (squamocolumnar junction (SCJ)-like and SCC, Fig S7B-C)(Camolotto et al., 2018). Both subtypes are more proliferative than both KF_1 and KF_1F_2 tumors and therefore contribute to the overall increase in tumor burden of KNF_1F_2 mice (Fig 7C).

To determine whether NKX2-1 loss can also rescue *Foxa1/2* KO in a p53-deficient context, we knocked down NKX2-1 (shNKX2-1; (Winslow et al., 2011)) alongside *Foxa1/2* KO in vitro (Fig 5A, 7D). NKX2-1 KD partially rescues the proliferation defect observed upon *Foxa1/2* KO in both cell lines and organoid cultures (Fig 7E-F). As expected (Snyder et al., 2013; Winslow et al., 2011), NKX2-1 knockdown also enhances proliferation in parental FoxA1/2+ cell lines and organoids. In order to determine whether NKX2-1 KD prevents tumor regression upon *Foxa1/2* KO, we subcutaneously injected NKX2-1 KD cells and treated tumor-bearing mice with either vehicle or tamoxifen. NKX2-1 KD increases the rate of growth in both the tamoxifen and vehicle treatments. Importantly, NKX2-1 KD largely prevents the tumor regression following *Foxa1/2* KO seen in the shScramble cohort (Fig 7G, S7D-E). Consistent with these rescue experiments, CRISPR-Cas9 mediated *FOXA1/2* KO in two NKX2-1-negative human LUAD cell lines (A549 and NCI-H2122) has no significant impact on growth (Fig S7F-G). Together, these data demonstrate that induction of aberrant NKX2-1 activity is one mechanism by which *Foxa1/2* KO inhibits LUAD growth.

DISCUSSION

LUAD progression is driven by epigenetic changes leading to increased plasticity relative to normal cells, which ultimately enables cancer cells to undergo profound changes in identity that enhance malignant potential (Boumahdi and de Sauvage, 2020; Campos-Parra et al., 2014; LaFave et al., 2020; Le Magnen et al., 2018; Marjanovic et al., 2020; Niederst et al., 2015; Quintanal-Villalonga et al., 2020; Russell, 2011; Sun and Yang, 2006; Tavernari et al., 2021; Travis et al., 2011). Here we show that FoxA1/2 coordinately drive multiple cell identity programs that are essential for LUAD progression. In the absence of FoxA1/2, LUAD cells undergo lineage switching to alternative non-proliferative cell fates (AT1, PATS, and SSSE). However, a subset of FoxA1/2-KO LUAD cells stochastically escape this proliferation arrest over time, undergoing an additional lineage switch (to either SCC or poorly differentiated, NKX2-1-negative LUAD) that enables them to regain their full malignant potential.

In NKX2-1+, p53-deficient LUAD, FoxA1/2 are required for expression of an AT2-like program and endodermal/GI programs. Moreover, we find that FoxA1/2 can activate both AT2 and GI gene networks within the same cancer cell. This is particularly striking because our previous work in a p53-proficient LUAD GEMM showed that FoxA1/2 are restricted to pulmonary activity when NKX2-1 is expressed, and can only activate GI targets upon NKX2-1 loss (Snyder et al., 2013). Mechanisms that promote expanded FoxA1/2 transcriptional activity in p53-deficient LUAD are unknown and will require additional investigation.

LUAD growth is highly dependent on FoxA1/2. *Foxa1/2* KO in autochthonous lung tumors, murine organoids, and human LUAD cell lines severely impedes proliferation, which in turn significantly increases survival. This strong dependence on FoxA1/2 is likely due to a combination of at least two distinct mechanisms, the first being the loss of a dual-identity state associated with progression into high grade disease. Additional studies are needed to determine how co-activation of GI and pulmonary programs in NKX2-1+ disease promotes tumor progression. Second, our data suggest that FoxA1/2-dependence in LUAD is also due to novel NKX2-1 activity that, in the absence of FoxA1/2, triggers the activation of TPs associated with non-proliferative cell types, including AT1 cells and maturing cells of the SSSE. Under normal conditions, both of these cell types require pools of other cell types to differentiate and replace them upon injury or death (AT2/PATS cells and basal epithelial stem cells, respectively). In further support of this hypothesis, KO of NKX2-1 alongside FoxA1/2 prevents the significant antiproliferative impact of *Foxa1/2* KO alone, as well as the emergence of these non-proliferative cell fates. These data suggest a model in which novel NKX2-1 transcriptional activity after *Foxa1/2* KO restrains tumor growth through the activation of alternative, non-proliferative cell identity programs. Nevertheless, there are likely additional mechanisms by which de novo NKX2-1 activity restrains LUAD growth following *Foxa1/2* KO that remain to be investigated.

In this study, we have laid the groundwork for several future directions. (1) This work clearly shows that FoxA1/2 are potential therapeutic targets. Whether it be through targeted degradation or the development of drugs that selectively inhibit FoxA proteins, our data show that blocking their transcriptional activity could improve outcomes for LUAD patients with NKX2-1+ disease. (2) Due to tumors developing resistance to *Foxa1/2* KO, it will be important to develop combinatorial strategies. We have shown that NKX2-1 actively inhibits growth following *Foxa1/2* KO in LUAD. It will be important to define the mechanism(s) by which NKX2-1 restrains tumor progression and ultimately identify therapeutic agents that might further augment the anti-tumor effects of NKX2-1 after FoxA1/2 inhibition. (3) Our work does not address the potential impact of FoxA1/2 inhibition on normal adult tissues, so it is also important to consider FoxA1/2 targets that activate GI TPs critical for tumor progression. Investigating these downstream targets, some of which may be directly druggable, in enforcing a dual-identity state is an important future direction and could yield a more clinically-actionable target.

Limitations of Study:

In this study we deleted *Foxa1/2* only in carcinoma cells. The potential impact of targeting FoxA1/2 systemically remains to be determined. Additionally, ChIPseq experiments were performed on organoids rather than in vivo tumors. It is possible that the TME influences relevant NKX2-1 and FoxA2 binding sites in vivo.

RESOURCE AVAILABILITY

Lead Contact

- Further information and requests for resources and reagents should be directed to and will be fulfilled by the lead contact, Eric Snyder (eric.snyder@hci.utah.edu)

Materials availability

- Novel murine cell lines and organoids are available upon request.
- The newly generated pCDH-EFS-FlpO lentivector will be deposited at Addgene.

Data and code availability

- Single-cell RNAseq, bulk RNAseq, and ChIPseq data have been deposited at Gene Expression Omnibus (GSE188438) and are publicly available as of the date of publication.
- This paper does not report original code.
- Any additional information required to reanalyze the data reported in this paper is available from the lead contact upon request.

EXPERIMENTAL MODEL AND SUBJECT DETAILS

Animal studies

Mice harboring *Kras*$^{FSF\text{-}G12D}$ (Young et al., 2011), *Braf*$^{FSF\text{-}V600E}$((Shai et al., 2015), *p53*^{frt}(Lee et al., 2012), *Rosa-FSF-Cre*^{ERT2} (Schonhuber et al., 2014), *Foxa1*^{flox} (Gao et al., 2008), *Foxa2*^{flox} (Sund et al., 2000), and *Nkx2-1*^{flox} (Kusakabe et al., 2006) have been previously described. All animals were maintained on a mixed 129/B6 background. All experimental mice were between 2 and 6 months of age at intubation. Mice of both sexes were used throughout each study. Animal studies were approved by the IACUC of the University of Utah, conducted in compliance with the Animal Welfare Act Regulations and other federal statutes relating to animals and experiments involving animals, and adhered to the principles set forth in the Guide for the Care and Use of Laboratory Animals, National Research Council (PHS assurance registration number A-3031-01).

Cell lines and primary cultures

All primary murine organoid cultures (see Key Resources Table) were established within Matrigel (Corning or Preclinical Research Shared Resource core facility) submerged in recombinant organoid medium for approximately two weeks (Advanced DMEM/F-12 supplemented with 1X B27 (Gibco), 1X N2 (Gibco), 1.25mM nAcetylcysteine (Sigma), 10mM Nicotinamide (Sigma), 10nM Gastrin (Sigma), 100ng/ml EGF (Peprotech), 100ng/ml R-spondin1 (Peprotech), 100ng/ml Noggin (Peprotech), and 100ng/ml FGF10 (Peprotech). After organoids were established, cultures were switched to 50% L-WRN conditioned media(Miyoshi and Stappenbeck, 2013).

A549, 3311, and HEK293T cells were cultured in DMEM/10% FBS (Gibco). NCI-H358, NCI-H441, NCI-H2009, and NCI-H2122 were cultured in RPMI/10% FBS (Gibco). NCI-H1651 was cultured in Advanced DMEM F-12/10% FBS (Gibco). All cell lines were tested periodically for mycoplasma contamination. To maintain cell cultures mycoplasma free, all culture media were supplemented with 2.5 ug/ml Plasmocin.

METHOD DETAILS

Tumor initiation, tamoxifen administration, and BrdU administration in vivo

Autochthonous lung tumors were initiated by administering viruses via intratracheal intubation. Adenoviral CMV-FlpO was used to initiate tumors in Figure 1A-C, and Supplemental Figure 1D-E, and I. Adenoviral mSPC-FlpO was used to initiate tumors in Supplemental Figure 1F, J, Figures 3-4, Figure 7B-C, and Supplemental Figure 7B-C. Lentiviral EFS-FlpO was used to initiate tumors in Figure 1D-E, Supplemental Figure 1G-H, Figure 7A, and Supplemental Figure 7A. Adenoviruses were obtained from University of Iowa Viral Vector Core. Lentivirus was generated as described in Lentiviral production and transduction methods section.

Tumor-specific activation of Cre^{ERT2} nuclear activity was achieved by intraperitoneal injection of tamoxifen (Sigma) dissolved in corn oil at a dose of 120mg/kg. Mice received 4 injections over the course of 5 days. For survival experiments, mice were additionally given pellets supplemented with 500mg/kg tamoxifen (Envigo) for 7 days following injections. BrdU incorporation was performed by injecting mice at 40mg/kg (Sigma) intraperitoneally 1 hour prior to tissue collection. Mice in survival studies were monitored for lethargy and respiratory distress, at which time animals were euthanized.

Analysis of human lung adenocarcinoma

IHC: Whole sections of de-identified formalin fixed, paraffin-embedded (FFPE) LUAD (n=42) were obtained from the Intermountain Biorepository, which collects samples in accordance with protocols approved by the Intermountain Healthcare Institutional Review Board. An additional 92 de-identified tumors were evaluated by FFPE tissue microarrays obtained from US Biomax (BC04115c and BCS04017).

TCGA: We first filtered all TCGA Pan Cancer Atlas lung adenocarcinoma samples based on high *NKX2-1* expression (*NKX2-1* z-score>−0.2, n=402/516 LUAD samples as of May 2022). The 402 *NKX2-1*-high samples were further filtered on *FOXA1* and *FOXA2* expression. We selected patients that had below average expression of both *FOXA1* and *FOXA2* for the *FOXA1/2*-low cohort (z-score<0 for both genes, n=23/402) and patients with above average expression of both *FOXA1* and *FOXA2* for the *FOXA1/2*-high cohort (z-score>0 for both genes; n=114/402). We identified differentially expressed genes between the *FOXA1/2*-high and *FOXA1/2*-low cohorts using DESeq2 and used the resultant log2FCs to run GSEA with our selected gene sets.

Histology and immunohistochemistry

All tissues were fixed in 10% formalin overnight and when necessary, lungs were perfused with formalin via the trachea. Organoids were first fixed in 10% formalin overnight and then mounted in HistoGel (Thermo Fisher Scientific). Mounted organoids and tissues were transferred to 70% ethanol, embedded in paraffin, and four-micrometer sections were cut. Immunohistochemistry (IHC) was performed manually on Sequenza slide staining racks (Thermo Fisher Scientific). Sections were treated with Bloxall (Vector Labs) followed by Horse serum 536 (Vector Labs) or Rodent Block M (Biocare Medical), primary antibody,

and HRP-polymer-conjugated secondary antibody (anti-Rabbit, Goat and Rat from Vector Labs; anti-Mouse from Biocare. The slides were developed with Impact DAB (Vector Labs) and counterstained with hematoxylin. Slides were stained with antibodies to FoxA1 (1:4000, Abcam 10881-14), FoxA2 (1:1200, Abcam 4466), Murine NKX2-1 (1:2000, Abcam EP1584Y), Human NKX2-1 (1:2000, Abcam 133638), BRDU (1:400, Abcam BU1/75), CC3 (CST 9664S 1:800), proSP-B (1:3000, Millipore AB3430), proSP-C (1:4000, Millipore AB3786), HNF4α (1:500, CST C11F12), ΔNp63 (1:100, Biocare [clone BC28]). Images were taken on a Nikon Eclipse Ni-U microscope with a DS-Ri2 camera and NIS-Elements software. Tumor Burden and BrdU quantitation and histological analyses were performed on hematoxylin and eosin-stained and IHC-stained slides using NIS-Elements software. All histopathologic analysis was performed by a board-certified anatomic pathologist (E.L.S.).

MicroCT imaging and analysis

Mice were anesthetized with isoflurane and imaged using a small animal Quantum GX2 microCT (Perkin Elmer). Images were acquired with 2 minute scans at 90 kV and 88-μA current, and reconstructed at a 90-μm voxel size. Resulting images were processed with Analyze 12.0 software (Analyze Direct) as described in Mollaoglu et al. 2017(Mollaoglu et al., 2017).

Establishing primary murine LUAD cell lines and organoids

Five months after tumor initiation in KF_1F_2 mice (2D cell lines; Lenti-CA2-FlpO-sh*p53*) and KPF_1F_2 mice (3D organoid lines; Adeno-mSPC-FlpO), tumor bearing mice were euthanized and lungs were isolated. Individual macroscopic tumors were removed from lungs, minced under sterile conditions, and digested at 37°C for 30 minutes with continuous agitation in a solution of Advanced DMEM/F12 containing the following enzymes: Collagenase Type I (Thermo Fisher Scientific, 450U/ml), Dispase (Corning, 5U/ml), DNaseI (Sigma, 0.25mg/ml). Enzyme reactions were stopped by addition of cold DMEM/F-12 with 10% FBS. The digested tissue was repeatedly passed through a 20-gauge syringe needle, sequentially dispersed through 100μm, 70 μm, and 40μm cell strainers, and treated with erythrocyte lysis buffer (eBioscience) to obtain a single cell suspension.

Standard cultures were established by seeding tumor cells in adherent culture flasks. Organoid cultures were established by seeding $1x10^5$ tumor cells in 50ul of Matrigel (Corning) and plated in 24-well plates. For the first 1-2 weeks of organoid initiation, Matrigel droplets were overlaid with recombinant organoid medium: Advanced DMEM/F-12 supplemented with 1X B27 (Gibco), 1X N2 (Gibco), 1.25mM nAcetylcysteine (Sigma), 10mM Nicotinamide (Sigma), 10nM Gastrin (Sigma), 100ng/ml EGF (Peprotech), 100ng/ml R-spondin1 (Peprotech), 100ng/ml Noggin (Peprotech), and 100ng/ml FGF10 (Peprotech). After organoids were established, cultures were switched to 50% L-WRN conditioned media(Miyoshi and Stappenbeck, 2013).

Organoid cultures were screened via immunohistochemistry and qPCR, and lines that uniformly expressed FoxA1, FoxA2, and NKX2-1 in all cells were selected for subsequent analysis. Standard culture cell lines were heterogeneous for NKX2-1, with both NKX2-1-positive and NKX2-1-negative cells identified within the same parental culture. In order to

generate uniform cultures for downstream analysis our 2D cell lines were single cell cloned. The clonal populations were screened via immunoblotting for FoxA1, FoxA2, and NKX2-1, and the cell line with strongest expression of all three transcription factors was selected for subsequent analysis. The full name of the 2D cell line in this paper labeled 3311 is 3311-Tumor 3-Subclone 1, which was shortened for clarity.

In vitro 4-hydroxytamoxifen treatment

Cells were transiently treated with 2μM 4-hydroxytamoxifen (Cayman Chemical Company, dissolved in 100% Ethanol) or vehicle for 48 (standard culture) or 72 (organoid culture) hours to activate CreER^{T2} nuclear activity and generate isogenic pairs.

Immunoblotting

Cells were lysed on ice for 20 minutes in RIPA buffer (50mM Tris HCl pH 7.4, 150 mM NaCl, 0.1 % (w/v) SDS, 0.5% (w/v) sodium deoxycholate, 1% (v/v) Triton X-100) plus complete protease phosphatase inhibitor cocktail (A32961, Thermo Fisher Scientific). Cellular debris was pelleted for 15 minutes at 4 °C and protein concentration was quantitated with the Coomassie (Bradford) Protein Assay (ThermoFisher Scientific). A total of 15μg (organoids) or 30μg (cell lines) of protein lysates were separated on Tris-Glycine (TGX) precast gels (BIO RAD) and transferred to nitrocellulose membranes (Thermo Fisher Scientific). Membranes were probed overnight with antibodies to FoxA1 (1:1000, Abcam 23738), FoxA2 (1:1000, Abcam 108422), NKX2-1 (1:2000, Abcam 133638), CC3 (CST 9664S 1:1000), and Vinculin (1:20000, Abcam 129002). The next day membranes were probed with IRDye 800CW Goat anti-Rabbit IgG Secondary Antibody (1:20000, LI-COR) and imaged with a LI-COR Odyssey CLx and Image Studio Software.

Generating a single cell suspension from organoid cultures

Matrigel droplets containing organoid cells were broken down via repeated pipetting in Cell Recovery Solution (Corning, 500μl per Matrigel droplet). Cell Recovery Solution containing organoids was transferred to sterile conical tubes and submerged in ice for 20-30 minutes before centrifugation at 4°C (300-500G). Cell Recovery Solution supernatant was removed and the cell pellet was washed via resuspension in PBS followed by centrifugation. Cells were then resuspended in pre-warmed TrypLE Express Enzyme (Thermo Fisher Scientific) and incubated for 5-7 minutes at 37°C. TrypLE reaction was quenched via dilution with cold Splitting Media (Advanced DMEM/F-12 [Gibco], 10 mM HEPES [Invitrogen], 1X Penicillin-Streptomycin-Glutamine [Invitrogen]). Cells were centrifuged and then resuspended in a pre-warmed DNase solution (L-WRN media supplemented to a final concentration of 200U/ml DNase [Worthington], 2.5 mM $MgCl_2$, 500 μM $CaCl_2$) and incubated for 5-7 minutes at 37°C. Cells were centrifuged and washed in PBS before use.

Cell viability and growth assays

Presto Blue Assay: Organoids were broken down into a single cell suspension and seeded at equal density with 5ul of Matrigel per well in a solid wall, clear bottom 96 well plate with 100ul of LWRN per well. One day after seeding, a baseline measurement was taken before beginning a 48 hour treatment with 4-OHT (or Ethanol). 10ul of PrestoBlue™

HS Cell Viability Reagent was added to each well and incubated at 37C for 1 hour. After incubation, fluorescent emission was quantified on a Synergy HTX plate reader (Excitation: 528/20, Emission: 590/20, Read: 560 emission). Presto blue reagent was removed and wells were washed with warm PBS before adding fresh LWRN media. Measurements were taken every other day until organoids reached confluency.

Incucyte Live-Cell Imaging: Standard culture cells were seeded at a density of 7,000 cells per well (3311), 10,000 cells per well (H1651, H2009 and A549), or 20,000 cells per well (H358, H441, and H2122) in a 96-well plate and grown within an IncuCyte Live Cell Imaging System. Wells were imaged every two hours. Percent phase confluence was determined using IncuCyte Zoom software. Culture media was changed as needed and the assay was ended once one of the conditions reached 100% confluency.

CellTiter-Glo Assay: Organoid cells were broken down into a single cell suspension. Four identical 48-well plates were seeded with three wells per condition (5000 cells/well in 15 ul of Matrigel). The following protocol was performed on the day of seeding, and every other day for 6 days following seeding. CellTiter-Glo 3D reagent (Promega) and 50% L-WRN media were warmed to room temperature. A working solution was prepared with a ratio of 1 part CTG:5 parts L-WRN. Media was removed from each well, 330 µl of CTG working solution was added to each well containing organoids and one empty well before shielding from light and incubating at room temperature for 30 minutes on a plate shaker at 500 RPM. After incubation CTG working solution was transferred to a clear-bottom, solid-wall 96 well plate (100ul/well; 3 wells/replicate; 3 replicates/sample). Luminescence was measured using an EnVision 2105 Multimode Plate Reader (Perkin Elmer). Luminescent signal for each condition was normalized to the corresponding Day 0 luminescence read.

Subcutaneous allografts

For subcutaneous allograft experiments, a single cell suspension of $3x10^5$ standard culture cells were mixed in a 1:1 volume with 50 µl of Matrigel. Cells were subcutaneously injected into the flank of NOD/SCID-gamma chain deficient mice (NSG). Tumor dimensions were measured with calipers, and tumor volume was calculated using the $(L \times W^2)/2$ formula. When the average volume of the tumors surpassed $200mm^3$, mice were randomized into Corn Oil or Tamoxifen cohorts (120mg/kg Tamoxifen). Mice received daily injections for 4 days. Tumor volume was monitored and measured every 3 days, and mice were euthanized once one tumor within the cohort surpassed $1000mm^3$ (Figure 1) or individually as their tumor volume surpassed $1000mm^3$ (Figure 4/4S).

Lentiviral production and transduction

Cloning of EFS-FlpO lentivector: We generated a pCDH-EFS-FlpO lentiviral vector by PCR amplifying the EFS (EF1a) promoter from the pCDH-Cre plasmid(Han et al., 2014), digesting the purified PCR product with XbaI, and cloning into SnaBI-XbaI sites of pCDH-CMV-FlpO(Camolotto et al., 2018) via ligation with T4 DNA ligase. Correct identity and orientation of the construct was confirmed via Sanger sequencing

In vivo use: HEK293T cells were transfected with EFS-FlpO-encoding lentiviral vector, Δ8.9 packaging vector, and VSV-G envelope vector mixed with TransIT-293 (Mirus) (DuPage et al., 2009). Virus-containing supernatant was collected 36, 48, 60, and 72 hours after transfection, and then ultracentrifuged at 25,000 RPM for 2 hours to concentrate virus for in vivo infection. The concentration of the final viral stock was determined using the mouse fibroblast FlpO-GFP reporter cell line 3TZ to determine Plaque Forming Units/μl (PFU).

Cloning of human dual sgRNA constructs: Dual targeting vectors were generated by inserting a sgRNA1-scaffold-bovineU6-sgRNA2 cassette (synthesized as gene-blocks by IDT) into the LRG2.1-GFP-P2A-BlastR vector using Gibson assembly. The scaffold sequence for sgRNA was generated by altering the stem-stem loop region of the LRG2.1 scaffold(Shi et al., 2015) based on previously described CRISPRi sgRNA scaffolds (Adamson et al., 2016). The sgRNA sequences used in this study are as follows:

sg*FOXA#1*: ATGTACGAGTAGGGCGGCT and TCGCCCGACAAGCCCGGCAA

sg*FOXA#10*: CCGTTCTCGAACATGTTGC and AGTCGTTGAAGGAGAGCGAG

sg*FOXA#11*: TGGACGCTGCACCCGGACTC and GCTCAGCGTCAGCATCTTGT

sgRosa: CCGGCGCCGAGCCGGACTTC and TTGCGGTCAGGTCACGCCGC.

In vitro use: HEK293T cells were transfected with lentiCRISPRv2 (Addgene Plasmid #98290), the above dual sgRNA constructs, pLKO.shNkx2-1 (Addgene Plasmid #32400) or pLKO.shScramble (Addgene Plasmid #1864) lentiviral vectors, Δ8.9 packaging vector, and VSV-G envelope vector mixed with TransIT-293 (Mirus). Virus-containing supernatant was collected 48, 60, and 72 hours after transfection, centrifuged to pellet floating HEK293T cells, and filtered using 0.45μm filters before storing long term at −80°C.

Human CRISPR/Cas9: Human cell lines were transduced with lentiCRISPRv2 by culturing with undiluted lentiviral media containing 8 μg/ml polybrene for 48 hours total, refreshing the media and polybrene at 24 hours. Three days after transduction ceased, cells were subjected to Puromycin selection to produce stable cell lines expressing Cas9. Cells were then transduced with lentiviral sgNT, sgFoxA#1, sgFoxA#10, or sgFoxA#11 and selected with Blasticidin in the same manner. After three days of selection, cells were seeded for an Incucyte proliferation assay, protein was collected for immunoblotting, and RNA was collected for qRT-PCR analysis.

shRNA: Standard culture cell lines were transduced by culturing with undiluted lentiviral media containing 8 μg/ml polybrene for 48 hours total, refreshing the media and polybrene at 24 hours. Three days after transduction ceased, cells were subjected to Puromycin selection to produce stable lines. For stable transduction of isogenic organoid pairs post-4OHT/Ethanol treatment, Matrigel domes containing organoids were resuspended in ice cold Splitting Media and centrifuged at 300G 4°C twice. Cells were then resuspended in TrypLE Express Enzyme (Thermo Fisher Scientific), incubated for 5 minutes at 37°C, and quenched with ice cold Splitting Media. Cell pellets were resuspended in a 1:1 mixture, by volume, of 50% L-WRN and lentiviral media with a final concentration of 8 μg/ml

polybrene, 1X Y-27632 (ROCK inhibitor), 1X A83-01 (ALK inhibitor), and 1X SB431542 (ALK inhibitor). The cell suspension was then transferred to a 6-well plate and centrifuged at 1700 RPM for 1 hour at room temperature. After centrifugation, the plate was incubated at 37°C for 2 hours. Cells were collected (scraping the bottom of the plate when necessary), centrifuged, resuspended in Matrigel, seeded in 24-well plates, and cultured in 50% L-WRN supplemented with 1X Y-27632, 1X A83-01, and 1X SB431542 for 72 hours. Three days after transduction, inhibitor media was washed away and cells were subjected to Puromycin selection to produce stable lines.

RNA Sequencing

RNA was collected from biological replicates of isogenic organoid cultures 1027B, 1027D, and 1292B 3 weeks after 4-OHT/Ethanol treatment. RNA was isolated via Trizol-chloroform extraction followed by column-based purification. The aqueous phase was brought to a final concentration of 50% ethanol, and RNA was purified using the PureLink RNA Mini kit according to the manufacturer's instructions (ThermoFisher Scientific). Library preparation was performed using the Illumina TruSeq Stranded mRNA Library Prep with UDI (Illumina; poly(A) selection). Sequencing was performed using the NovaSeq 6000 (50 x 50 bp paired-end sequencing; 25 million reads per sample).

RNAseq Data Processing and Analysis

The mouse GRCm38 genome and gene feature files were downloaded from Ensembl release 102 and a reference database was created using STAR version 2.7.6a(Dobin et al., 2013). Optical duplicates were removed from NovaSeq runs via Clumpify v38.34(Bushnell, 2021). Reads were trimmed of adapters and aligned to the reference database using STAR in two pass mode to output a BAM file sorted by coordinates. Mapped reads were assigned to annotated genes using featureCounts version 1.6.3(Liao et al., 2019). Raw counts were filtered to remove features with zero counts and features with five or fewer reads in every sample. Differentially expressed genes were identified using a 5% false discovery rate with DESeq2 version 1.34.0(Love et al., 2014). For each genotype, we ran a separate model using Condition + Line in the design formula to compare 4-OHT vs EtOH while controlling for cell line effects on gene expression.

GSEA-Preranked was run with the differential gene list generated from DESeq2 and the following MSigDB gene sets: c2, c3, c4, c5, c6, c8, and Hallmarks on May 4, 2022. Gene sets smaller than 15 and larger than 500 were excluded from analysis. Marjanovic et al Clusters and Program gene lists and ADI/PATS signatures were downloaded from their supplemental materials.

Evaluation of NKX2-1 dependence—We first performed differential gene expression analysis (DESeq2) between the following pairs of samples: (1) shScramble vehicle treated (FoxA1/2-positive; NKX2-1-positive) vs shScramble tamoxifen treated (FoxA1/2-negative; NKX2-1-positive) (2) shScramble vehicle treated (FoxA1/2-positive; NKX2-1-positive) vs shNKX2-1 tamoxifen treated (FoxA1/2-negative; NKX2-1-knock down). We then intersected the differential gene lists for these two comparisons. Gene expression changes found in both comparisons were deemed NKX2-1 independent because the expression

change is induced upon *Foxa1/2* deletion regardless of NKX2-1 levels. Gene expression changes unique to comparison (1) were deemed NKX2-1 dependent because the expression change induced upon *Foxa1/2* deletion only occurs when NKX2-1 is fully expressed.

Single Cell RNA Sequencing

Mice were injected with tamoxifen 10 weeks after intubation and single cells were collected 12 weeks after intubation as follows. Lungs and heart were perfused with PBS. Individual macroscopic tumors were removed from the lungs and broken down into single cell suspensions as described in Establishing primary murine LUAD cell lines and organoids methods. Pre-depletion cells were viably cryopreserved in 5% DMSO/FBS. The remaining cells were depleted of CD45-positive and CD31-positive cells using MACS with Miltenyi microbeads (CD45: 130-052-301; CD31: 130-097-418) and LD columns (130-042-901) following manufacturer recommendations. Post-depletion cells were viably cryopreserved in 5% DMSO/FBS.

Protocols used to generate scRNA-seq data with 10x Genomics Chromium platform can be found at https://support.10xgenomics.com/single-cell-gene-expression.

In brief, the Chromium Single Cell Gene Expression Solution with 3’ chemistry, version 3 (PN-1000075) was used to barcode individual cells with 16bp 10X barcodes and to tag cell specific transcript molecules with 10bp Unique Molecular Identifier (UMI) according to the manufacturer’s instructions. The following protocol was performed at the High-Throughput Genomics Shared Resource at Huntsman Cancer Institute, University of Utah. Single cells were suspended in phosphate buffered saline with 0.04% bovine serum albumin, and the cell suspension was passed through a 40 micron cell strainer. Viability and cell count were assessed on Countess II (Thermo Scientific). Suspensions were equilibrated to targeted cell recovery of 8000 cells. For the KP sample without stromal depletion, the targeted cell recovery was 7500 cells. 10x Gel Beads and reverse transcription reagents were added and cell suspensions were loaded to Chromium Single Cell A (PN-120236) to form Gel Beads-in emulsions (GEMs) - the nano-droplets. Within individual GEMs, cDNA generated from captured and barcoded mRNA was synthesized by reverse transcription at the setting of 53°C for 45 min followed by 85°C for 5 min. Subsequent A tailing, end repair, adaptor ligation and sample indexing were performed in bulk according to the manufacturer’s instructions. The resulting barcoding libraries were qualified on Agilent D1000 ScreenTape on Agilent Technology 2200 TapeStation system and quantified by quantification PCR using KAPA Biosystems Library Quantification Kit for Illumine Platforms (KK4842). Multiple libraries were then normalized and sequenced on NovaSeq 6000 with 2 × 150 PE mode.

scRNAseq Data Processing and Analysis

Demultiplexing and data alignment—Single-cell RNA-seq data from both KP (n=2) and KPF_1F_2 (n=2) tumors were demultiplexed using the 10x cellranger mkfastq version 3.1.0 to create fastq files with the I1 sample index, R1 cell barcode+UMI, and R2 sequence. Reads were aligned to the mouse genome (mm10 with custom CRE-ERT2 and FoxA1/2 individual exon references) and UMIs were generated using cellranger count 3.1.0 with expected-cells set to 8000 per library. For the KP sample without stromal depletion,

expected-cells was set to 7500. QC reporting, clustering, and dimension reduction were performed for initial data evaluation in 10x Genomics' Cell Loupe Browser (v5.0). For the KP sample without stromal depletion, we captured 5,963 cells total with 48,090 mean reads per cell and 1,488 median genes per cell. For the KP sample with stromal depletion, we captured 8,536 cells total with 25,593 mean reads per cell and 736 median genes per cell. For the KPF_1F_2 sample without stromal depletion, we captured 4,662 cells total with 55,589 mean reads per cell and 1,552 median genes per cell. For the KPF_1F_2 sample with stromal depletion, we captured 4,415 cells total with 60,226 mean reads per cell and 1,339 median genes per cell. Additional details of the primary Cell Ranger data processing can be found at: https://support.10xgenomics.com/single-cell-gene-expression/software/pipelines/latest/algorithms/overview.

Quality control, clustering, and cell type identification—Single cell expression data was subjected to common Seurat workflows for initial quality control and clustering (https://satijalab.org/seurat/articles/pbmc3k_tutorial.html). Cells with unique feature counts over 7500 or less than 200 and over 20% mitochondrial counts were filtered out for downstream analysis. Counts of cells passing QC were then log normalized and scaled based on all genes using Seurat's NormalizeData and ScaleData functions. PCA linear dimension reduction was performed and Seurat's FindNeighbors function was employed to embed single cell profiles in a K-nearest neighbor (KNN) graph based on a (30 PC) PCA space. The FindClusters function was utilized to iteratively group cells together using Louvian algorithm modularity optimization techniques. Clustering was performed based on the top 30 dimensions using Seurat's RunUMAP function. Differentially expressed genes for each cluster were identified using Seurat's FindMarkers function using default setting. The Mouse Cell Atlas' scMCA R package was run with the top differentially expressed genes for each cluster (Supplemental Table 2) to facilitate cell type identification. Following QC filtering and tumor cell identification, 4646 KP and 2481 KPF1F2 high quality tumor cells remained. For subsequent analyses, identified tumor cells from KP and KPF1F2 tumors were subsetted out and reclustered based on the top 25 dimensions. Cell barcodes identified as tumor cells that were used for downstream analyses are included in Supplemental Table 3. Reclustering of identified tumor cells in UMAP space revealed 13 clusters (Figure 3A) To identify KPF_1F_2 complete recombinants, expression of the floxed second exon of Foxa1 was visualized (Figure 3C).

Differential gene expression and signature score assignment—Differentially expressed genes in each of the tumor cell clusters were calculated using Seurat's FindMarkers function. Differentially expressed genes of UMAP clusters from all KP and KPF_1F_2 tumor cells can be found in Supplemental Table 3. Gene module scores for several published gene signatures for AT1 cells AT2 cells(Du et al., 2015; Little et al., 2019; Marjanovic et al., 2020; Travaglini et al., 2020), and various additional cell types and states including stratified squamous epithelium (MSigDB) were determined per cell across the tumor cell and complete recombinant data sets using Seurat's AddModuleScore function. Gene lists for each of these scores can be found in Supplemental Table 5.

Chromatin Immunoprecipitation Sequencing

Organoids were broken down into a single cell suspension before following the manufacturer protocol v1.5 for Chromatrap ChIP-seq Protein A kits (500189) with the following modifications/optimizations:

Step 1 (Chromatin preparation, fixation, collection): Broken down, individual organoid cells were treated as suspension cells for crosslinking.

Step 2 (Cell lysis and chromatin shearing): Crosslinked cells were suspended in 100ul of Lysis Buffer/2,000,000 cells. Sonication was performed with 20 cycles of 30 seconds on:30 seconds off at 70% to reach fragmentation of 100-500bp lengths. Input DNA was purified with Zymo ChIP DNA Clean and Concentrator columns (D5205). DNA concentration was determined using Qubit dsDNA High Sensitivity Assay Kit (Q32851).

Step 3 (Slurry preparation and immunoprecipitation): NKX2-1 IP was performed with a sample:antibody ratio of 10ug sample:4.2ug antibody (Abcam ab133737). FoxA2 IP was performed with a sample:antibody ratio of 10ug sample: 5ug antibody (CST D56D6 custom high concentration formulation)

Step 4 (Reverse cross-linking): IP DNA was purified with Zymo ChIP DNA Clean and Concentrator columns (D5205).

IP and input samples were prepared for sequencing with NEBNext Ultra II DNA Library Prep Kit and sequenced on an Illumina Novaseq 6000 as paired-end 150 bp reads (HCI High-Throughput Genomics core).

ChIPseq Data Processing and Analysis

Samples were de-multiplexed with Illumina BCL2Fastq using dual indexes and single bp mismatch. Fastq reads were aligned to the standard chromosomes of mouse genome, version mm10, using Novocraft novoalign (v4.03.01 http://www.novocraft.com) with provided tuned settings for Novaseq. Sequence adapter sequences were provided to Novoalign for masking during alignment. Alignment pairings were checked with samtools (v1.10) fixmate function.

Samples were run through the MultiRepMacsChIPSeq pipeline (v17 https://github.com/HuntsmanCancerInstitute/MultiRepMacsChIPSeq) with five independent samples. After comparison, four replicates were chosen for analysis, based on correlation metrics and number of peaks identified. Briefly, the pipeline consists of the following steps. Exclusion intervals representing high-copy genomic sequences were first generated by calling peaks on combined, unfiltered Input samples. Any alignments overlapping exclusion intervals were discarded from further analysis. Only properly-paired alignments were used; chimeric and singleton alignments were discarded. Duplicate alignments based on coordinates were randomly subsampled to a final rate of 5% across all samples from a mean of 24% (range 18-32%). Peaks were called individually for each replicate using MACS2 (v2.2.6 https://github.com/macs3-project/MACS) with peak calling parameters of qvalue 0.01, min-length 200 bp, max-gap 100 bp, and genome size (empirically determined) 2554209000 bp. Called peaks were first combined between replicates for each condition, EtOH and Tamoxifen treated, and then combined into a master peak list for both conditions using BEDtools

(v2.28.0 https://bedtools.readthedocs.io). Mean fragment coverage tracks were generated using bam2wig (BioToolBox, v1.68 https://github.com/tjparnell/biotoolbox) by first depth-normalizing to 1 million paired-end fragments, then averaging between replicates. Multi-mapping alignments were scaled by the number of genomic hits reported by the aligner. Mean Log2 Fold Enrichment tracks were generated by using MACS2 bdgcmp function with depth-normalized ChIP coverage and generated mean lambda control coverage tracks, then converting to base 2 log values with manipulate_wig (BioToolBox). Count tracks were generated with bam2wig scaling to a total depth of 20M fragments, the lowest observed depth amongst all samples.

Peaks were scored using get_datasets (BioToolBox) with the depth-normalized count files generated by the MultiRepMacsChIPSeq pipeline. Fractional fragment counts were rounded to the nearest integer for simplicity. Differential peaks were identified by running MAnorm2(Tu et al., 2021) with recommended parameters, using “parametric” for fitting the mean variance curve and initial coefficients of 0.1 and 10. Differential peaks were identified by a padj value < 0.05. Data was collected for peaks by using BED files of the peaks of interest using the BioToolBox (v1.68) programs get_relative_data, using 50 bins of 40 bp surrounding the peak midpoint (±1 kb). Heat maps and plots were generated with custom R scripts using pHeatmap (https://cran.r-project.org/package=pheatmap) and ggplot2 (https://ggplot2.tidyverse.org). Peaks were annotated with ChIPseeker(Yu et al., 2015) and Ensembl gene annotation (release 98), restricted to expressed, protein-coding, Gencode transcripts. Motifs, both known and novel, were identified using the Homer package (http://homer.ucsd.edu/homer/).

QUANTIFICATION AND STATISTICAL ANALYSIS

All graphing and statistical analysis was performed with PRISM software, with all graphs showing mean and standard deviation. The statistical details can be found in the corresponding figure legend. All NGS statistical analysis was performed according to published pipeline protocols cited, with a statistical significance cutoff of padj<0.05.

Supplementary Material

Refer to Web version on PubMed Central for supplementary material.

Acknowledgements:

We are grateful to members of the Snyder lab for suggestions and comments. We thank Brian Dalley for sequencing expertise, Jay Gertz for ChIPseq expertise, and Kaylyn Bauer for immunology expertise. The results published here are in part based upon data generated by the TCGA Research Network: https://www.cancer.gov/tcga. ELS was supported grants from NIH (R01CA212415 and R01CA240317), the Burroughs Wellcome Fund, and institutional funds. CRV was supported by Pershing Square Sohn Cancer Research Alliance, the Cold Spring Harbor Laboratory and Northwell Health Affiliation, the National Cancer Institute 5P01CA013106-Project 4 and 1R01CA229699, the Thompson Family Foundation, the Simons Foundation, and a Career Development Award from the Pancreatic Cancer Action Network–American Association for Cancer Research 16-20-25-VAKO. GO was supported by the NIH/NCI (F31CA243427) and the Eunice Kennedy Shriver National Institute of Child Health & Human Development (T32HD007491). OK was supported by the Deutsche Forschungsgemeinschaft (DFG) Research Fellowship (KL 3228/1-1). Research reported in this publication utilized shared resources (including High Throughput Genomics, Bioinformatics, and Biorepository and Molecular Pathology) at the University of Utah and was supported by the National Cancer Institute of the National Institutes of Health under Award Number

P30CA042014. The content is solely the responsibility of the authors and does not necessarily represent the official views of the NIH.

REFERENCES

Adamson B, Norman TM, Jost M, Cho MY, Nunez JK, Chen Y, Villalta JE, Gilbert LA, Horlbeck MA, Hein MY, et al. (2016). A Multiplexed Single-Cell CRISPR Screening Platform Enables Systematic Dissection of the Unfolded Protein Response. Cell 167, 1867–1882 e1821. 10.1016/j.cell.2016.11.048. [PubMed: 27984733]

Bachurski CJ, Yang GH, Currier TA, Gronostajski RM, and Hong D (2003). Nuclear factor I/thyroid transcription factor 1 interactions modulate surfactant protein C transcription. Mol Cell Biol 23, 9014–9024. 10.1128/MCB.23.24.9014-9024.2003. [PubMed: 14645514]

Bejarano PA, Baughman RP, Biddinger PW, Miller MA, Fenoglio-Preiser C, al-Kafaji B, Di Lauro R, and Whitsett JA (1996). Surfactant proteins and thyroid transcription factor-1 in pulmonary and breast carcinomas. Mod Pathol 9, 445–452. [PubMed: 8729987]

Bernardo GM, and Keri RA (2012). FOXA1: a transcription factor with parallel functions in development and cancer. Biosci Rep 32, 113–130. 10.1042/BSR20110046. [PubMed: 22115363]

Besnard V, Wert SE, Hull WM, and Whitsett JA (2004). Immunohistochemical localization of Foxa1 and Foxa2 in mouse embryos and adult tissues. Gene Expr Patterns 5, 193–208. 10.1016/j.modgep.2004.08.006. [PubMed: 15567715]

Bingle CD (1997). Thyroid transcription factor-1. Int J Biochem Cell Biol 29, 1471–1473. [PubMed: 9570141]

Boggaram V (2009). Thyroid transcription factor-1 (TTF-1/Nkx2.1/TITF1) gene regulation in the lung. Clin Sci (Lond) 116, 27–35. 10.1042/CS20080068. [PubMed: 19037882]

Bohinski RJ, Di Lauro R, and Whitsett JA (1994). The lung-specific surfactant protein B gene promoter is a target for thyroid transcription factor 1 and hepatocyte nuclear factor 3, indicating common factors for organ-specific gene expression along the foregut axis. Mol Cell Biol 14, 5671–5681. [PubMed: 8065304]

Boumahdi S, and de Sauvage FJ (2020). The great escape: tumour cell plasticity in resistance to targeted therapy. Nat Rev Drug Discov 19, 39–56. 10.1038/s41573-019-0044-1. [PubMed: 31601994]

Bushnell B (2021). BBtools.

Camolotto SA, Pattabiraman S, Mosbruger TL, Jones A, Belova VK, Orstad G, Streiff M, Salmond L, Stubben C, Kaestner KH, and Snyder E (2018). FoxA1 and FoxA2 drive gastric differentiation and suppress squamous identity in NKX2-1-negative lung cancer. Elife 7. 10.7554/eLife.38579.

Campos-Parra AD, Aviles A, Contreras-Reyes S, Rojas-Marin CE, Sanchez-Reyes R, Borbolla-Escoboza RJ, and Arrieta O (2014). Relevance of the novel IASLC/ATS/ERS classification of lung adenocarcinoma in advanced disease. Eur Respir J 43, 1439–1447. 10.1183/09031936.00138813. [PubMed: 24435003]

Casanova-Acebes M, Dalla E, Leader AM, LeBerichel J, Nikolic J, Morales BM, Brown M, Chang C, Troncoso L, Chen ST, et al. (2021). Tissue-resident macrophages provide a pro-tumorigenic niche to early NSCLC cells. Nature 595, 578–584. 10.1038/s41586-021-03651-8. [PubMed: 34135508]

Cha YJ, and Shim HS (2017). Biology of invasive mucinous adenocarcinoma of the lung. Transl Lung Cancer Res 6, 508–512. 10.21037/tlcr.2017.06.10. [PubMed: 29114467]

Choi J, Park JE, Tsagkogeorga G, Yanagita M, Koo BK, Han N, and Lee JH (2020). Inflammatory Signals Induce AT2 Cell-Derived Damage-Associated Transient Progenitors that Mediate Alveolar Regeneration. Cell Stem Cell 27, 366–382 e367. 10.1016/j.stem.2020.06.020. [PubMed: 32750316]

Dobin A, Davis CA, Schlesinger F, Drenkow J, Zaleski C, Jha S, Batut P, Chaisson M, and Gingeras TR (2013). STAR: ultrafast universal RNA-seq aligner. Bioinformatics 29, 15–21. 10.1093/bioinformatics/bts635. [PubMed: 23104886]

Du Y, Guo M, Whitsett JA, and Xu Y (2015). 'LungGENS': a web-based tool for mapping single-cell gene expression in the developing lung. Thorax 70, 1092–1094. 10.1136/thoraxjnl-2015-207035. [PubMed: 26130332]

DuPage M, Dooley AL, and Jacks T (2009). Conditional mouse lung cancer models using adenoviral or lentiviral delivery of Cre recombinase. Nat Protoc 4, 1064–1072. 10.1038/nprot.2009.95. [PubMed: 19561589]

Engblom C, Pfirschke C, Zilionis R, Da Silva Martins J, Bos SA, Courties G, Rickelt S, Severe N, Baryawno N, Faget J, et al. (2017). Osteoblasts remotely supply lung tumors with cancer-promoting SiglecF(high) neutrophils. Science 358. 10.1126/science.aal5081.

Gao B, Xie W, Wu X, Wang L, and Guo J (2020). Functionally analyzing the important roles of hepatocyte nuclear factor 3 (FoxA) in tumorigenesis. Biochim Biophys Acta Rev Cancer 1873, 188365. 10.1016/j.bbcan.2020.188365. [PubMed: 32325165]

Gao N, LeLay J, Vatamaniuk MZ, Rieck S, Friedman JR, and Kaestner KH (2008). Dynamic regulation of Pdx1 enhancers by Foxa1 and Foxa2 is essential for pancreas development. Genes Dev 22, 3435–3448. 10.1101/gad.1752608. [PubMed: 19141476]

Han X, Li F, Fang Z, Gao Y, Li F, Fang R, Yao S, Sun Y, Li L, Zhang W, et al. (2014). Transdifferentiation of lung adenocarcinoma in mice with Lkb1 deficiency to squamous cell carcinoma. Nat Commun 5, 3261. 10.1038/ncomms4261. [PubMed: 24531128]

Herriges JC, Yi L, Hines EA, Harvey JF, Xu G, Gray PA, Ma Q, and Sun X (2012). Genome-scale study of transcription factor expression in the branching mouse lung. Dev Dyn 241, 1432–1453. 10.1002/dvdy.23823. [PubMed: 22711520]

Hight SK, Mootz A, Kollipara RK, McMillan E, Yenerall P, Otaki Y, Li LS, Avila K, Peyton M, Rodriguez-Canales J, et al. (2020). An in vivo functional genomics screen of nuclear receptors and their co-regulators identifies FOXA1 as an essential gene in lung tumorigenesis. Neoplasia 22, 294–310. 10.1016/j.neo.2020.04.005. [PubMed: 32512502]

Jin S, Guerrero-Juarez CF, Zhang L, Chang I, Ramos R, Kuan CH, Myung P, Plikus MV, and Nie Q (2021). Inference and analysis of cell-cell communication using CellChat. Nat Commun 12, 1088. 10.1038/s41467-021-21246-9. [PubMed: 33597522]

Kaestner KH (2010). The FoxA factors in organogenesis and differentiation. Curr Opin Genet Dev 20, 527–532. 10.1016/j.gde.2010.06.005. [PubMed: 20591647]

Kobayashi Y, Tata A, Konkimalla A, Katsura H, Lee RF, Ou J, Banovich NE, Kropski JA, and Tata PR (2020). Persistence of a regeneration-associated, transitional alveolar epithelial cell state in pulmonary fibrosis. Nat Cell Biol 22, 934–946. 10.1038/s41556-020-0542-8. [PubMed: 32661339]

Kusakabe T, Kawaguchi A, Hoshi N, Kawaguchi R, Hoshi S, and Kimura S (2006). Thyroid-specific enhancer-binding protein/NKX2.1 is required for the maintenance of ordered architecture and function of the differentiated thyroid. Mol Endocrinol 20, 1796–1809. 10.1210/me.2005-0327. [PubMed: 16601074]

LaFave LM, Kartha VK, Ma S, Meli K, Del Priore I, Lareau C, Naranjo S, Westcott PMK, Duarte FM, Sankar V, et al. (2020). Epigenomic State Transitions Characterize Tumor Progression in Mouse Lung Adenocarcinoma. Cancer Cell 38, 212–228 e213. 10.1016/j.ccell.2020.06.006. [PubMed: 32707078]

Le Magnen C, Shen MM, and Abate-Shen C (2018). Lineage Plasticity in Cancer Progression and Treatment. Annu Rev Cancer Biol 2, 271–289. 10.1146/annurev-cancerbio-030617-050224. [PubMed: 29756093]

Lee CL, Moding EJ, Huang X, Li Y, Woodlief LZ, Rodrigues RC, Ma Y, and Kirsch DG (2012). Generation of primary tumors with Flp recombinase in FRT-flanked p53 mice. Dis Model Mech 5, 397–402. 10.1242/dmm.009084. [PubMed: 22228755]

Li CM, Gocheva V, Oudin MJ, Bhutkar A, Wang SY, Date SR, Ng SR, Whittaker CA, Bronson RT, Snyder EL, et al. (2015). Foxa2 and Cdx2 cooperate with Nkx2-1 to inhibit lung adenocarcinoma metastasis. Genes Dev 29, 1850–1862. 10.1101/gad.267393.115. [PubMed: 26341558]

Liao Y, Smyth GK, and Shi W (2019). The R package Rsubread is easier, faster, cheaper and better for alignment and quantification of RNA sequencing reads. Nucleic Acids Research 47, e47–e47. 10.1093/nar/gkz114. [PubMed: 30783653]

Little DR, Gerner-Mauro KN, Flodby P, Crandall ED, Borok Z, Akiyama H, Kimura S, Ostrin EJ, and Chen J (2019). Transcriptional control of lung alveolar type 1 cell development and maintenance by NK homeobox 2-1. Proc Natl Acad Sci U S A 116, 20545–20555. 10.1073/pnas.1906663116. [PubMed: 31548395]

Little DR, Lynch AM, Yan Y, Akiyama H, Kimura S, and Chen J (2021). Differential chromatin binding of the lung lineage transcription factor NKX2-1 resolves opposing murine alveolar cell fates in vivo. Nat Commun 12, 2509. 10.1038/s41467-021-22817-6. [PubMed: 33947861]

Liu C, Glasser SW, Wan H, and Whitsett JA (2002). GATA-6 and thyroid transcription factor-1 directly interact and regulate surfactant protein-C gene expression. J Biol Chem 277, 4519–4525. 10.1074/jbc.M107585200. [PubMed: 11733512]

Love MI, Huber W, and Anders S (2014). Moderated estimation of fold change and dispersion for RNA-seq data with DESeq2. Genome Biol 15, 550. 10.1186/s13059-014-0550-8. [PubMed: 25516281]

Maier B, Leader AM, Chen ST, Tung N, Chang C, LeBerichel J, Chudnovskiy A, Maskey S, Walker L, Finnigan JP, et al. (2020). A conserved dendritic-cell regulatory program limits antitumour immunity. Nature 580, 257–262. 10.1038/s41586-020-2134-y. [PubMed: 32269339]

Marjanovic ND, Hofree M, Chan JE, Canner D, Wu K, Trakala M, Hartmann GG, Smith OC, Kim JY, Evans KV, et al. (2020). Emergence of a High-Plasticity Cell State during Lung Cancer Evolution. Cancer Cell 38, 229–246 e213. 10.1016/j.ccell.2020.06.012. [PubMed: 32707077]

Meza R, Meernik C, Jeon J, and Cote ML (2015). Lung cancer incidence trends by gender, race and histology in the United States, 1973-2010. PLoS One 10, e0121323. 10.1371/journal.pone.0121323. [PubMed: 25822850]

Minoo P, Hu L, Xing Y, Zhu NL, Chen H, Li M, Borok Z, and Li C (2007). Physical and functional interactions between homeodomain NKX2.1 and winged helix/forkhead FOXA1 in lung epithelial cells. Mol Cell Biol 27, 2155–2165. 10.1128/MCB.01133-06. [PubMed: 17220277]

Miyoshi H, and Stappenbeck TS (2013). In vitro expansion and genetic modification of gastrointestinal stem cells in spheroid culture. Nature Protocols 8, 2471–2482. 10.1038/nprot.2013.153. [PubMed: 24232249]

Mollaoglu G, Guthrie MR, Bohm S, Bragelmann J, Can I, Ballieu PM, Marx A, George J, Heinen C, Chalishazar MD, et al. (2017). MYC Drives Progression of Small Cell Lung Cancer to a Variant Neuroendocrine Subtype with Vulnerability to Aurora Kinase Inhibition. Cancer Cell 31, 270–285. 10.1016/j.ccell.2016.12.005. [PubMed: 28089889]

Mollaoglu G, Jones A, Wait SJ, Mukhopadhyay A, Jeong S, Arya R, Camolotto SA, Mosbruger TL, Stubben CJ, Conley CJ, et al. (2018). The Lineage-Defining Transcription Factors SOX2 and NKX2-1 Determine Lung Cancer Cell Fate and Shape the Tumor Immune Microenvironment. Immunity 49, 764–779 e769. 10.1016/j.immuni.2018.09.020. [PubMed: 30332632]

Moses MA, George AL, Sakakibara N, Mahmood K, Ponnamperuma RM, King KE, and Weinberg WC (2019). Molecular Mechanisms of p63-Mediated Squamous Cancer Pathogenesis. Int J Mol Sci 20. 10.3390/ijms20143590.

Niederst MJ, Sequist LV, Poirier JT, Mermel CH, Lockerman EL, Garcia AR, Katayama R, Costa C, Ross KN, Moran T, et al. (2015). RB loss in resistant EGFR mutant lung adenocarcinomas that transform to small-cell lung cancer. Nat Commun 6, 6377. 10.1038/ncomms7377. [PubMed: 25758528]

Paranjapye A, Mutolo MJ, Ebron JS, Leir SH, and Harris A (2020). The FOXA1 transcriptional network coordinates key functions of primary human airway epithelial cells. Am J Physiol Lung Cell Mol Physiol 319, L126–l136. 10.1152/ajplung.00023.2020. [PubMed: 32432922]

Quintanal-Villalonga A, Chan JM, Yu HA, Pe'er D, Sawyers CL, Sen T, and Rudin CM (2020). Lineage plasticity in cancer: a shared pathway of therapeutic resistance. Nat Rev Clin Oncol 17, 360–371. 10.1038/s41571-020-0340-z. [PubMed: 32152485]

Robinson JL, Holmes KA, and Carroll JS (2013). FOXA1 mutations in hormone-dependent cancers. Front Oncol 3, 20. 10.3389/fonc.2013.00020. [PubMed: 23420418]

Russell PAW. Z; Wright GM; Daniels M; Conron M; Williams RA (2011). Does lung adenocarcinoma subtype predict patient survival?: A clinicopathologic study based on the new International Association for the Study of Lung Cnacer/American Thoracic Society/European Respiratory Society international multidisciplinary lung adenocarcinoma classification. Journal of thoracic oncology: official publication of the International Association for the Study of Lung Cnacer, 1496–1504.

Schonhuber N, Seidler B, Schuck K, Veltkamp C, Schachtler C, Zukowska M, Eser S, Feyerabend TB, Paul MC, Eser P, et al. (2014). A next-generation dual-recombinase system for time- and host-specific targeting of pancreatic cancer. Nat Med 20, 1340–1347. 10.1038/nm.3646. [PubMed: 25326799]

Shai A, Dankort D, Juan J, Green S, and McMahon M (2015). TP53 Silencing Bypasses Growth Arrest of BRAFV600E-Induced Lung Tumor Cells in a Two-Switch Model of Lung Tumorigenesis. Cancer Res 75, 3167–3180. 10.1158/0008-5472.CAN-14-3701. [PubMed: 26001956]

Shi J, Wang E, Milazzo JP, Wang Z, Kinney JB, and Vakoc CR (2015). Discovery of cancer drug targets by CRISPR-Cas9 screening of protein domains. Nat Biotechnol 33, 661–667. 10.1038/nbt.3235. [PubMed: 25961408]

Snyder EL, Watanabe H, Magendantz M, Hoersch S, Chen TA, Wang DG, Crowley D, Whittaker CA, Meyerson M, Kimura S, and Jacks T (2013). Nkx2-1 represses a latent gastric differentiation program in lung adenocarcinoma. Molecular cell 50, 185–199. 10.1016/j.molcel.2013.02.018. [PubMed: 23523371]

Strunz M, Simon LM, Ansari M, Kathiriya JJ, Angelidis I, Mayr CH, Tsidiridis G, Lange M, Mattner LF, Yee M, et al. (2020). Alveolar regeneration through a Krt8+ transitional stem cell state that persists in human lung fibrosis. Nat Commun 11, 3559. 10.1038/s41467-020-17358-3. [PubMed: 32678092]

Sun Z, and Yang P (2006). Gene expression profiling on lung cancer outcome prediction: present clinical value and future premise. Cancer Epidemiol Biomarkers Prev 15, 2063–2068. 10.1158/1055-9965.EPI-06-0505. [PubMed: 17119029]

Sund NJ, Ang SL, Sackett SD, Shen W, Daigle N, Magnuson MA, and Kaestner KH (2000). Hepatocyte nuclear factor 3beta (Foxa2) is dispensable for maintaining the differentiated state of the adult hepatocyte. Mol Cell Biol 20, 5175–5183. [PubMed: 10866673]

Tavernari D, Battistello E, Dheilly E, Petruzzella AS, Mina M, Sordet-Dessimoz J, Peters S, Krueger T, Gfeller D, Riggi N, et al. (2021). Nongenetic Evolution Drives Lung Adenocarcinoma Spatial Heterogeneity and Progression. Cancer Discov 11, 1490–1507. 10.1158/2159-8290.CD-20-1274. [PubMed: 33563664]

Teng M, Zhou S, Cai C, Lupien M, and He HH (2021). Pioneer of prostate cancer: past, present and the future of FOXA1. Protein & Cell 12, 29–38. 10.1007/s13238-020-00786-8. [PubMed: 32946061]

Travaglini KJ, Nabhan AN, Penland L, Sinha R, Gillich A, Sit RV, Chang S, Conley SD, Mori Y, Seita J, et al. (2020). A molecular cell atlas of the human lung from single-cell RNA sequencing. Nature 587, 619–625. 10.1038/s41586-020-2922-4. [PubMed: 33208946]

Travis WD, Brambilla E, Noguchi M, Nicholson AG, Geisinger KR, Yatabe Y, Beer DG, Powell CA, Riely GJ, Van Schil PE, et al. (2011). International association for the study of lung cancer/american thoracic society/european respiratory society international multidisciplinary classification of lung adenocarcinoma. J Thorac Oncol 6, 244–285. 10.1097/JTO.0b013e318206a221. [PubMed: 21252716]

Tu S, Li M, Chen H, Tan F, Xu J, Waxman DJ, Zhang Y, and Shao Z (2021). MAnorm2 for quantitatively comparing groups of ChIP-seq samples. Genome Res 31, 131–145. 10.1101/gr.262675.120. [PubMed: 33208455]

Varma S, Cao Y, Tagne JB, Lakshminarayanan M, Li J, Friedman TB, Morell RJ, Warburton D, Kotton DN, and Ramirez MI (2012). The transcription factors Grainyhead-like 2 and NK2-homeobox 1 form a regulatory loop that coordinates lung epithelial cell morphogenesis and differentiation. J Biol Chem 287, 37282–37295. 10.1074/jbc.M112.408401. [PubMed: 22955271]

Watanabe H, Francis JM, Woo MS, Etemad B, Lin W, Fries DF, Peng S, Snyder EL, Tata PR, Izzo F, et al. (2013). Integrated cistromic and expression analysis of amplified NKX2-1 in lung adenocarcinoma identifies LMO3 as a functional transcriptional target. Genes Dev 27, 197–210. 10.1101/gad.203208.112. [PubMed: 23322301]

Winslow MM, Dayton TL, Verhaak RG, Kim-Kiselak C, Snyder EL, Feldser DM, Hubbard DD, DuPage MJ, Whittaker CA, Hoersch S, et al. (2011). Suppression of lung adenocarcinoma progression by Nkx2-1. Nature 473, 101–104. 10.1038/nature09881. [PubMed: 21471965]

Yang D, Jones MG, Naranjo S, Rideout WM, Min KH, Ho R, Wu W, Replogle JM, Page JL, Quinn JJ, et al. (2021). Lineage Recording Reveals the Phylodynamics, Plasticity and Paths of Tumor Evolution. bioRxiv, 2021.2010.2012.464111. 10.1101/2021.10.12.464111.

Yi M, Tong GX, Murry B, and Mendelson CR (2002). Role of CBP/p300 and SRC-1 in transcriptional regulation of the pulmonary surfactant protein-A (SP-A) gene by thyroid transcription factor-1 (TTF-1). J Biol Chem 277, 2997–3005. 10.1074/jbc.M109793200. [PubMed: 11713256]

Young NP, Crowley D, and Jacks T (2011). Uncoupling cancer mutations reveals critical timing of p53 loss in sarcomagenesis. Cancer Res 71, 4040–4047. 10.1158/0008-5472.CAN-10-4563. [PubMed: 21512139]

Yu G, Wang LG, and He QY (2015). ChIPseeker: an R/Bioconductor package for ChIP peak annotation, comparison and visualization. Bioinformatics 31, 2382–2383. 10.1093/bioinformatics/btv145. [PubMed: 25765347]

Zilionis R, Engblom C, Pfirschke C, Savova V, Zemmour D, Saatcioglu HD, Krishnan I, Maroni G, Meyerovitz CV, Kerwin CM, et al. (2019). Single-Cell Transcriptomics of Human and Mouse Lung Cancers Reveals Conserved Myeloid Populations across Individuals and Species. Immunity 50, 1317–1334 e1310. 10.1016/j.immuni.2019.03.009. [PubMed: 30979687]

- FoxA1/2 are required for growth in NKX2-1-positive lung adenocarcinoma
- FoxA1/2 activate a dual identity cellular state critical in LUAD tumor evolution
- FoxA1/2 suppress non-proliferative cellular states driven by novel NKX2-1 activity
- NKX2-1 actively represses growth following FoxA1/2 deletion

Lung adenocarcinoma evolution relies on epigenetic changes that confer increased lineage plasticity. Orstad et. al. show that transcription factors FoxA1 and FoxA2 are critical drivers of LUAD growth and transcriptional evolution. FoxA1/2 restrain the activity of NKX2-1; following Foxa1/2 deletion, NKX2-1 actively inhibits tumor growth by promoting non-proliferative cell fates.

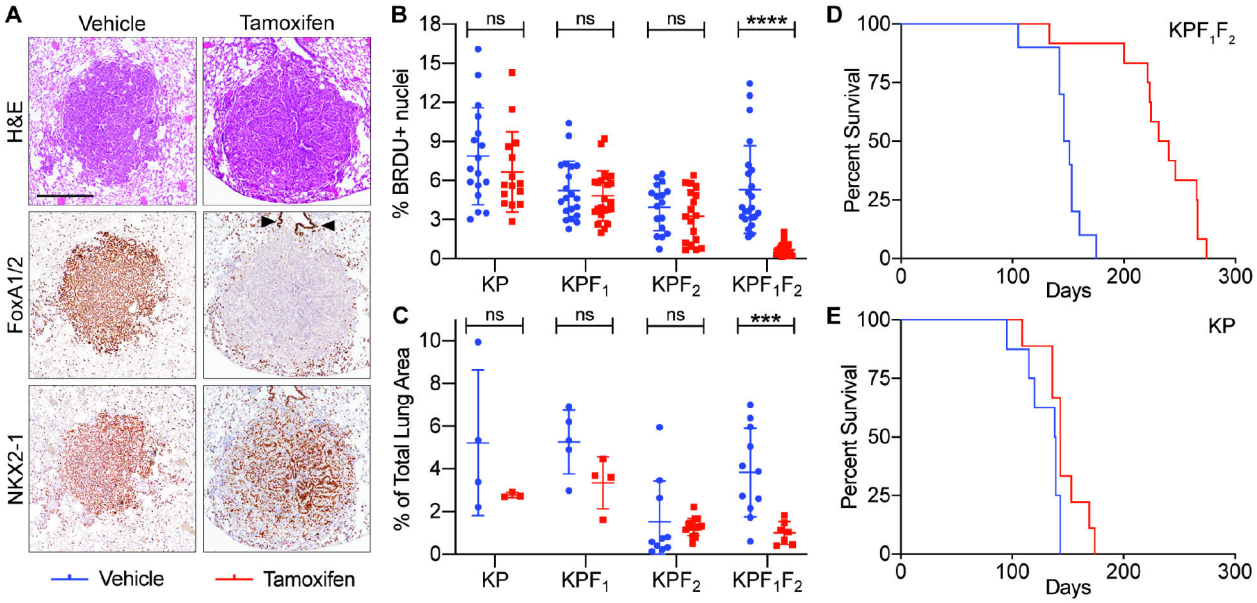

Figure 1: FoxA1/2 are required for LUAD growth in vivo

A) Representative images of KPF_1F_2 tumors. IHC for FoxA1/2 and NKX2-1 and Hematoxylin and Eosin (H&E) staining shown. Arrowheads mark FoxA1/2+ normal bronchiolar epithelium, confirming tumor-specific KO of FoxA1/2 (scale bar 1000 μm) **B)** BRDU IHC quantification of individual KP, KPF_1, KPF_2, and KPF_1F_2 tumors treated with tamoxifen or vehicle 6 weeks post-initiation and collected at 8 weeks (****p<0.0001, unpaired t-test). **C)** Tumor burden quantification of individual mice from the experiment shown in B (***p=0.001014, unpaired t-test) **D)** KPF_1F_2 survival study, Median survival of Vehicle is 21.2 weeks (n=10). Tamoxifen is 34.7 weeks (n=12; p<0.0001, Log-rank Mantel-Cox test) **E)** KP survival study in which vehicle (blue, n=8) or tamoxifen (red, n=9) was administered 10 weeks post-initiation. Median survival of Vehicle is 19.8 weeks (n=8). Tamoxifen is 20.4 weeks (n=9; p=0.0645)

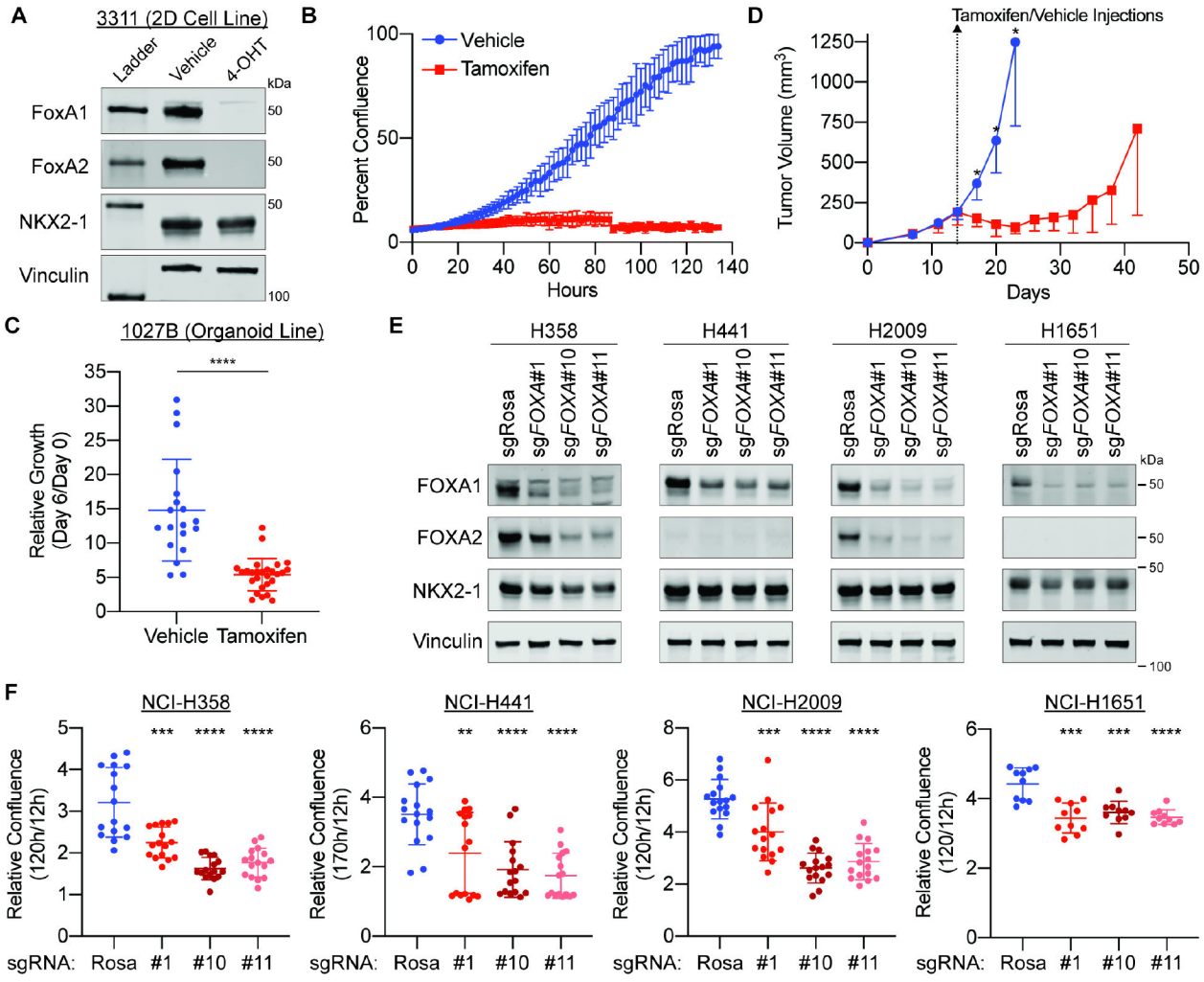

Figure 2: FoxA1/2 are required for LUAD growth in vitro

A) Western blot of a KPF_1F_2 cell line collected 3 days post 48-hour 4-OHT treatment **B)** Incucyte-based growth assay of 3311 1 week post-treatment (one representative replicate shown of n=3 biological replicates; p<0.0001 unpaired t-test of endpoint values) **C)** Presto Blue proliferation assay of a KPF_1F_2 organoid line 6 days post 48-hour vehicle or 4-OHT treatment (p<0.0001 unpaired t-test) **D)** Subcutaneous tumors (3311) were allowed to grow to an average of 200mm^3 before treating with either vehicle (n=5) or tamoxifen (n=5) (unpaired t-test day 17 p=0.0027; day 20 p=0.0006; day 23 p=0.0012; mean+SD of one of two independent experiments shown) **E)** Western blots of human LUAD cell lines stably expressing Cas9 transduced with three separate lentivectors that express sgRNAs targeting FOXA1 and FOXA2 (sg*FOXA*#1, sg*FOXA*#10, and sg*FOXA*#11), as well as a dual sgRNA control targeting the Rosa locus (sgRosa) **F)** Normalized percent confluence in Incucyte-based growth assay (n=2 biological replicates; unpaired t-test relative to sgRosa **p<0.005, ***p<0.001, ****p<0.0001)

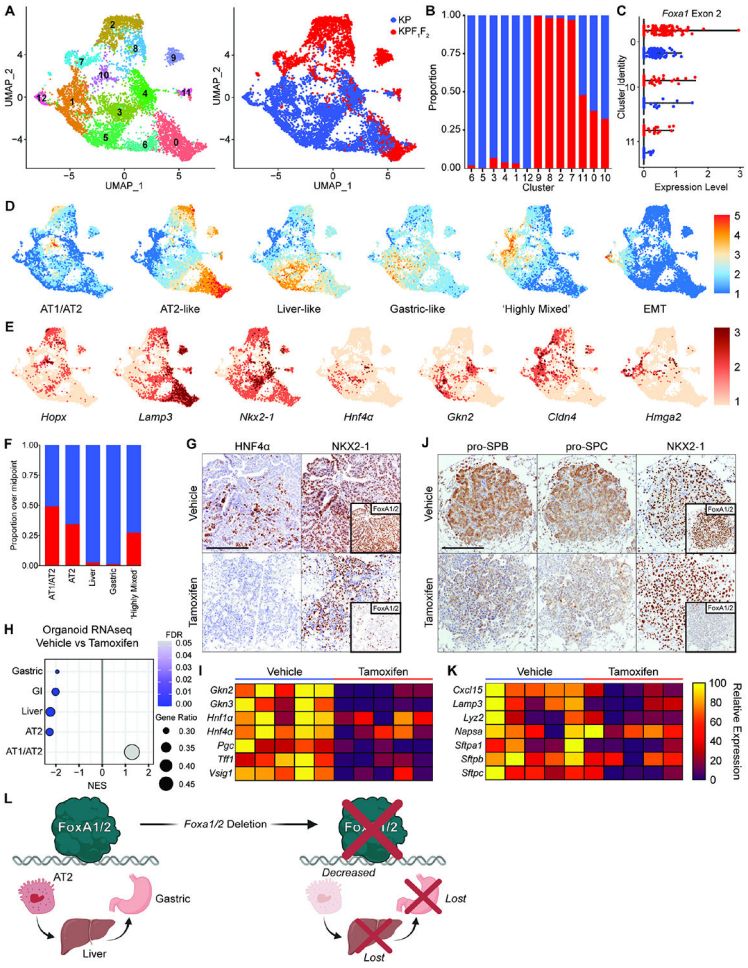

Figure 3: FoxA1/2 enforce AT2 and GI-related transcriptional programs

A) UMAP of cells from KP (4646 cells) and KPF_1F_2 (2481 cells) tumors (n=2 mice per genotype, multiple tumors per mouse). Left panel colored by cluster identity and right by genotype **B)** Proportion of cells in each cluster from KP or KPF_1F_2 tumors **C)** Expression of *Foxa1*'s 2nd exon that should be excised by Cre-ERT2. Detection of this exon within KPF_1F_2 cells indicates retained expression of *Foxa1/2* due to incomplete Cre recombination **D)** UMAPs of gene module scores of dual-identity TPs associated with tumor progression and **E)** relative expression of genes corresponding to above TPs **F)** Proportion of FoxA1/2+/KO cells with gene module scores at or over the median **G)** IHC of gastric TF HNF4α and pulmonary TF NKX2-1 **H)** Normalized Enrichment Score (NES) of organoid RNAseq GSEA. Positive NES indicates enrichment in FoxA1/2-KO organoids and negative NES indicates enrichment in FoxA1/2+ organoids. Gene ratio representing the proportion of genes within a gene signature detected in the DEG list **I)** Expression of gastric marker genes in vehicle and 4-OHT treated organoids **J)** IHC of AT2 markers pro-SPB, pro-SPC, and pulmonary TF NKX2-1 **K)** Expression of AT2-specific genes in vehicle and 4-OHT treated organoids **L)** Summary image created in BioRender (all scale bars 500 μm)

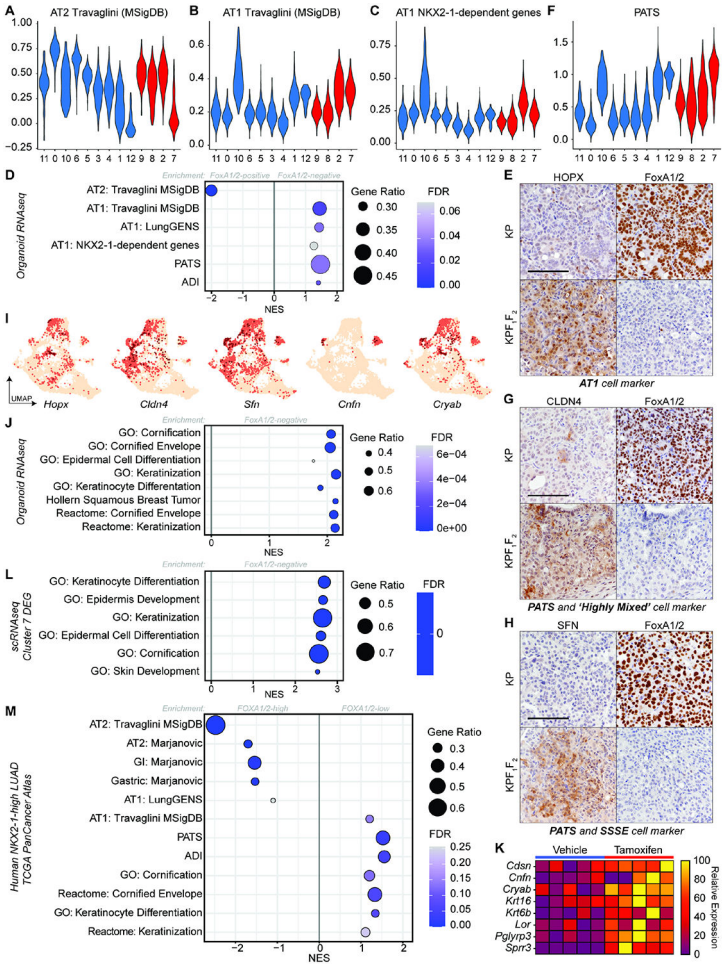

Figure 4: FoxA1/2 suppress alternative pulmonary and stratified squamous transcriptional programs

A) Violin plots representing the expression of the Travaglini AT2, **B)** Travaglini AT1 and **C)** NKX2-1-dependent AT1 TPs in each tumor cell cluster. Y-axis indicates gene module score. X-axis indicates cluster identity **D)** Alveolar TP GSEA of KPF_1F_2 organoid RNAseq **E)** IHC for AT1 marker HOPX in KP and KPF_1F_2 tumors **F)** PATS TP expression in tumor cell clusters **G)** IHC for PATS and 'Highly Mixed' marker CLDN4 and **H)** PATS and SSSE marker SFN (all scale bars 250 μm) **I)** UMAPs showing expression of AT1, PATS, and SSSE genes in tumor cells (AT1: *Hopx* and *Cryab*; PATS: *Cldn4* and *Sfn*; SSSE: *Sfn, Cnfn,* and *Cryab*) **J)** SSSE TP GSEA of KPF_1F_2 organoid RNAseq **K)** Expression of SSSE genes in vehicle and 4-OHT treated organoids **L)** GSEA of FoxA1/2-KO scRNAseq C7 **M)** GSEA of DEGs between *FOXA1/2*-high and *FOXA1/2*-low cohorts in in *NKX2-1*-high human LUAD patients (TCGA Pan Cancer Atlas)

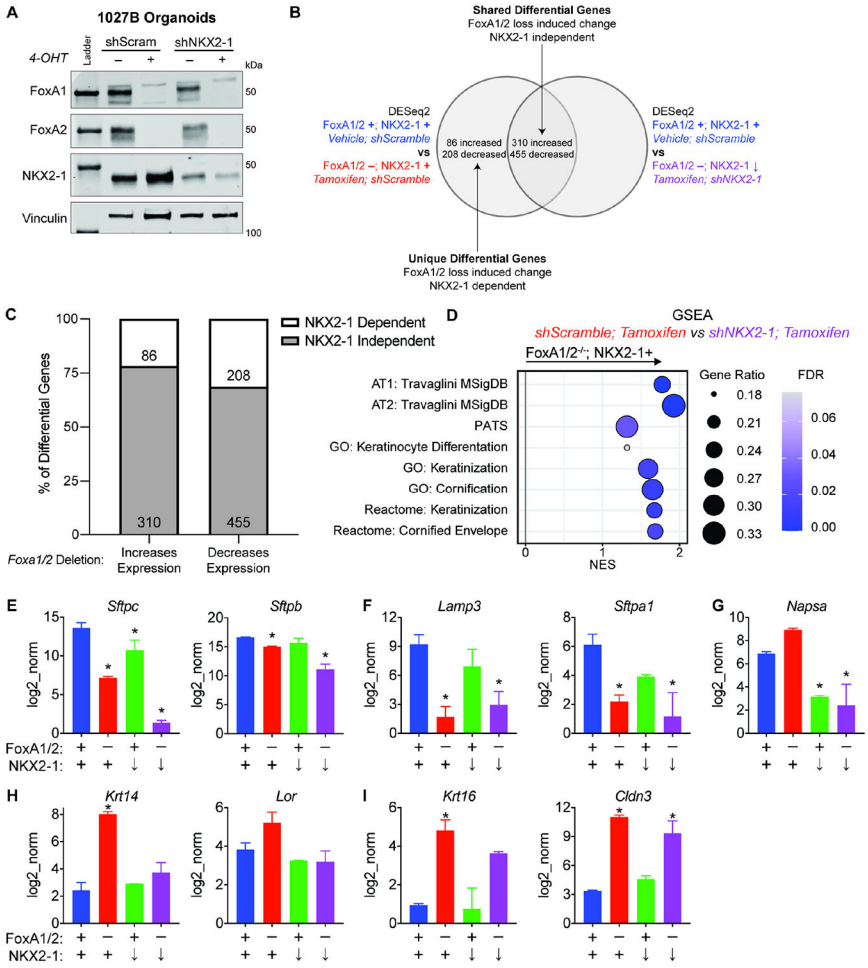

Figure 5: NKX2-1 is required for a subset of gene expression changes induced by FoxA1/2 loss

A) Western blot of organoids transduced with shScramble and shNKX2-1 and then treated with 4-OHT/vehicle **B)** Graphical representation of relevant comparisons for data shown in Figure 5C. See methods section for detailed description of bioinformatic analysis **C)** Number of DEGs following *Foxa1/2* KO in 1027B categorized by NKX2-1 dependence **D)** GSEA of DEGs between FoxA1/2-KO; NKX2-1+ and FoxA1/2-KO; NKX2-1-KD organoids **E)** Normalized expression of AT2 genes that show additive FoxA1/2 and NKX2-1 function: *Sftpc* and *Sftpb* (*padj<0.007), **(F)** are primarily dependent on FoxA1/2 function: *Lamp3* and *Sftpa1* (*padj<$2x10^{-5}$), **(G)** or are dependent on NKX2-1 and not FoxA1/2: *Napsa* (*padj<$7.22x10^{-10}$) **H)** Normalized expression of SSSE genes that are dependent on NKX2-1: *Krt14* and *Lor* (*padj<$7.22x10^{-17}$) or **I)** independent of NKX2-1: *Krt16* and *Cldn3* (*padj<0.006)

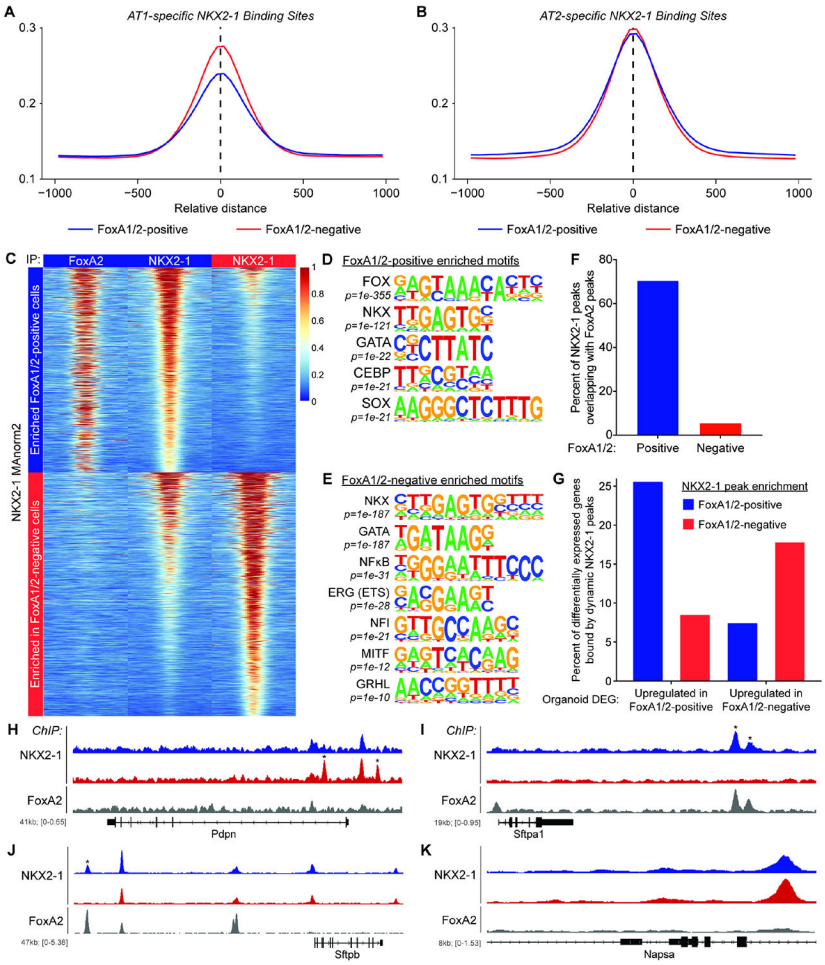

Figure 6: FoxA1/2 regulate global NKX2-1 binding in LUAD

A) Mean peak profile of FoxA1/2+ and FoxA1/2 KO NKX2-1 ChIP peaks over all AT1-specific and **B)** AT2-specific NKX2-1 binding sites (n=4 biological replicates of NKX2-1 ChIPseq in FoxA1/2+ and FoxA1/2-KO organoids) **C)** Heatmap of FoxA2 peaks (left) and NKX2-1 peaks at the loci of 2,758 differential NKX2-1 binding sites as determined by MAnorm2 (significance cutoff of padj<0.05) in FoxA1/2+ (center) and FoxA1/2-KO (right) organoids **D)** TF motifs detected in NKX2-1 peaks enriched in FoxA1/2+ or **E)** FoxA1/2-KO organoids **F)** Proportion of differential NKX2-1 peaks that overlap with a FoxA2 peak **G)** Association between differential NKX2-1 binding and DEGs (p<0.0001, Fishers exact test) **H)** FoxA2 and NKX2-1 ChIP peaks in FoxA1/2+ and FoxA1/2-KO organoids at AT1 marker *Pdpn* and AT2 markers **I)** *Sftpa1*, **J)** *Sftpb*, and **K)** *Napsa*

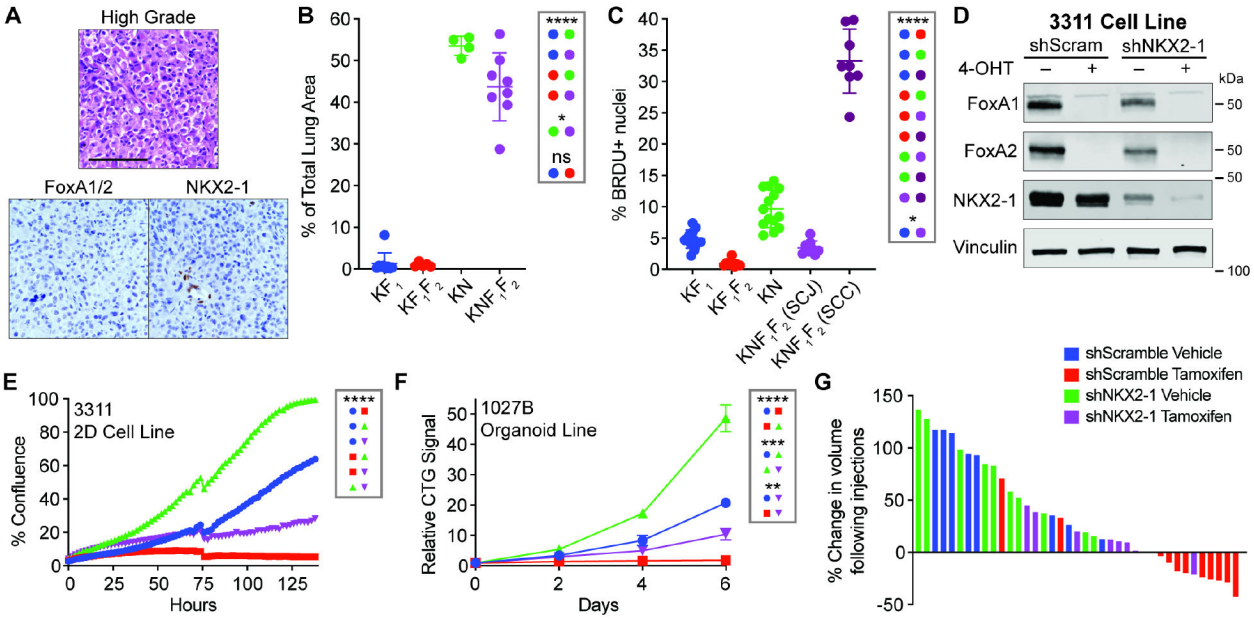

Figure 7: NKX2-1 restrains tumor growth in the absence of FoxA1/2

A) High grade, NKX2-1-negative tumors that emerged in the FoxA1/2 KO cohort of long-term survival studies. Top panel H&E, bottom panels IHC (scale bar 250 μm) **B)** Tumor burden of KF_1, KF_1F_2, KN, and KNF_1F_2 mice (unpaired t-tests; *p=0.0424; ****p<0.0001) **C)** BRDU quantification of experiment shown in B (unpaired t-tests; *p=0.0366; ****p<0.0001) **D)** Western blot of a KPF_1F_2 cell line transduced with shScramble and shNKX2-1 collected 3 days post 48-hour 4-OHT/vehicle treatment **E)** Incucyte-based confluency growth assay of cells shown in D one week after 4-OHT/vehicle treatment. One of two biological replicates shown (unpaired t-tests of endpoints; ****p<0.0001) **F)** CellTiter-Glo 3D growth assay of organoids in Fig 5A. Normalized to day 0 luminescence reads for each condition. One of two biological replicates shown (unpaired t-tests of endpoints; **p=0.0016; ***p<0.0005; ****p<0.0001) **G)** Change in subcutaneous tumor volumes. Tumor volume after completion of tamoxifen/vehicle injections relative to volume immediately preceding treatment.

REAGENT or RESOURCE	SOURCE	IDENTIFIER
Antibodies		
Rabbit monoclonal to FoxA1 (IHC)	Abcam	ab173286 [EPR10881-14]
Rabbit polyclonal to FoxA1 (WB)	Abcam	ab23738
Rabbit monoclonal to FoxA2 (WB; IHC)	Abcam	ab108422 [EPR4466]
Rabbit monoclonal to FoxA2 (ChIPseq)	Cell Signaling Technologies	Cat#8186 (D56D6)
Rabbit monoclonal to NKX2-1 (Murine IHC)	Abcam	ab76013 [EP1584Y]
Rabbit monoclonal to NKX2-1 (WB; Human IHC)	Abcam	ab133638 [EPR8190-6]
Rabbit monoclonal to NKX2-1 (ChIPseq)	Abcam	ab133737 [EPR5955(2)]
Rat monoclonal to BRDU	Abcam	ab6326 [BU1/75 (ICR1)]
Rabbit polyclonal to proSP-B	Millipore	AB3430
Rabbit polyclonal to proSP-C	Millipore	AB3786
Rabbit monoclonal to HNF4a	Cell Signaling Technologies	Cat#3113 (C11F12)
Mouse monoclonal to p40 (DNp63)	Biocare	Cat#BC28
Rabbit monoclonal to Vinculin	Abcam	ab129002 [EPR8185]
Rabbit polyclonal to HOPX	Abcam	ab230544
Rabbit polyclonal to CLDN4	Invitrogen	ZMD.306
Rabbit polyclonal to SFN	Sigma Aldrich	HPA01105
Rabbit monoclonal to CC3	Cell Signaling Technologies	Cat#9664
IRDye 800CW Goat anti-Rabbit IgG Secondary Antibody	Licor	925-332211
Bacterial and Virus Strains		
Stbl3	Thermo Fisher	C737303
Ad5CMV-Flpo	University of Iowa Gene Transfer Vector Core	530-HT
Ad5mSPC-Flpo	University of Iowa Gene Transfer Vector Core	Snyder-6695
Biological Samples		
Human Tumor Microarrays	US Biomax	BC04115c and BCS04017
Chemicals, peptides, and recombinant proteins		
4-Hydroxytamoxifen	Cayman Chemicals	Cat#17308
Tamoxifen	Sigma Aldrich	Cat#T5648
Collagenase Type I	Thermo Fisher Scientific	Cat#17100-017
Dispase	Corning	Cat#354235
DNase I	Sigma Aldrich	Cat#DN25
B-27	Gibco	Cat#17504044
N-2	Gibco	Cat#17502048
nAcetylcysteine	Sigma Aldrich	Cat#A7250
Nicotinamide	Sigma Aldrich	Cat#N3376
Gastrin I	Sigma Aldrich	Cat#G9020
Murine EGF	PeproTech	Cat#315-09

REAGENT or RESOURCE	SOURCE	IDENTIFIER
Murine R-Spondin-1	PeproTech	Cat#315-32
Murine Noggin	PeproTech	Cat#250-38
Human FGF-10	PeproTech	Cat#100-26
Polybrene	Sigma Aldrich	Cat#107689
Y-27632	Tocris	Cat# 1254
A83-01	Tocris	Cat# 2939
SB431542	Tocris	Cat# 1614
DMEM, high glucose	Thermo Fisher Scientific	Cat# 11965118
Advanced DMEM/F12	Thermo Fisher Scientific	Cat# 12634028
RPMI 1640	Thermo Fisher Scientific	Cat# 11875119
Penicillin-Streptomycin-Glutamine	Gibco	Cat# 10378016
TrypLE Express Enzyme	Thermo Fisher Scientific	Cat# 12604021
Cell Recovery Solution	Corning	Cat# 10378016
HEPES	Gibco	Cat# 15630080
DNase	Worthington	Cat# LS002006
TransIT-293	Mirus	Cat# MIR2700
Critical commercial assays		
PrestoBlue HS Cell Viability Assay	Thermo Fisher Scientific	Cat# P50200
CellTiter-Glo 3D	Promega	Cat# G9681
LunaScript RT Supermix	NEB	Cat# E3010
Luna Universal Probe qPCR Master Mix	NEB	Cat# M3004
SFTPA1 qPCR Probe	Thermo Fisher Scientific	Cat# Hs00831305_s1
SFTPB qPCR Probe	Thermo Fisher Scientific	Cat# Hs01090667_m1
Pierce Coomassie (Bradford) Protein Assay Kit	Thermo Fisher Scientific	Cat# 23200
PureLink RNA Mini Kit	Thermo Fisher Scientific	Cat# 12183018A
Illumina TruSeq Stranded mRNA Library Prep with UDI	Illumina	Cat# 20020595
CD45 Microbeads	Miltenyi Biotec	Cat #130-052-301
CD31 Microbeads	Miltenyi Biotec	Cat# 130-097-418
LD MACS Columns	Miltenyi Biotec	Cat# 130-042-901
Chromatrap ChIP-seq Protein A Kits	Chromatrap	Cat# 500189
NEBNext Ultra II DNA Library Prep Kit	NEB	Cat# E7645
Qubit dsDNA HS Assay Kit	Invitrogen	Cat# Q32854
ChIP DNA Clean & Concentrator	Zymo Research	Cat# 11-379C
PureLink Quick Plasmid Miniprep Kit	Invitrogen	Cat# K210011
PureLink HiPure Plasmid Filter Maxiprep Kit	Invitrogen	Cat# K210017
BLOXALL® Endogenous Blocking Solution, Peroxidase and Alkaline Phosphatase	Vector Labs	Cat#SP-6000-100
ImPRESS HRP Horse Anti-Rabbit IgG Polymer Detection Kit, Peroxidase	Vector Labs	Cat#MP-7401
ImPRESS Goat Anti-Rat IgG (Mouse Adsorbed) Polymer Kit, Peroxidase	Vector Labs	Cat#MP-7444

REAGENT or RESOURCE	SOURCE	IDENTIFIER
Rodent Block M	Biocare Medical	Cat#RBM961G
Mouse-on-Mouse HRP Polymer	Biocare Medical	Cat#MM620
Deposited Data		
RNAseq, scRNAseq, and ChIPseq data for this study	NCBI Gene Expression Omnibus	GSE188438
Uncropped western blot images	Mendeley Data	DOI:10.17632/mc4xkprx7h.1
TCGA Pan Cancer Atlas	GDC DTT	N.A.
Mouse Cell Atlas 2.0	Ming Chen and Guoji Guo	2.0
Little et al 2021 NKX2-1 ChIPseq and ATACseq	NCBI Gene Expression Omnibus	GSE158205
Experimental models: Cell lines		
L-WRN: *Mus musculus* (Male)	ATCC	Cat#CRL-3276
293T: *Homo sapiens* (Fetus)	ATCC	Cat#CRL-3216
NCI-H2009: *Homo sapiens* (Female)	ATCC	Cat#CRL-5911
NCI-H441: *Homo sapiens* (Male)	ATCC	Cat#HTB-174
NCI-H358: *Homo sapiens* (Male)	ATCC	Cat#CRL-5807
NCI-H1651: *Homo sapiens* (Male)	ATCC	Cat#CRL-5884
NCI-H2122: *Homo sapiens* (Female)	ATCC	Cat#CRL-5985
A549: *Homo sapiens* (Male)	ATCC	Cat#CCL-185
3311: *Mus musculus* (Female)	This paper	N.A.
1027B: *Mus musculus* (Female)	This paper	N.A.
1027D: *Mus musculus* (Female)	This paper	N.A.
1292B: Mus musculus (Female)	This paper	N.A.
1552A: *Mus musculus* (Male)	This paper	N.A.
1552B: *Mus musculus* (Male)	This paper	N.A.
1552C: *Mus musculus* (Male)	This paper	N.A.
1267B: *Mus musculus* (Male)	This paper	N.A.
1526C: *Mus musculus* (Female)	This paper	N.A.
Experimental models: Organisms/strains		
Braf$^{FSF\text{-}V600E}$/+: *Mus musculus* mixed C57BJ/6J x 129SvJ background	Dr. Martin McMahon (HCI, Salt Lake City, UT)	Shai et al 2015 PMID:26001956
Kras$^{FSF\text{-}G12D}$/+: *Mus musculus* mixed C57BL/6J x 129SvJ background	Dr. Tyler Jacks (MIT, Cambridge, MA)	Young et al 2011 PMID:21512139
Trp53$^{FRT/FRT}$: *Mus musculus* mixed C57BL/6J x 129SvJ background	Dr. David G Kirsch (Duke University, Durham, NC)	Lee et al 2012 PMID:22228755
Rosa$^{FSF\text{-}CreERT2}$: *Mus musculus* mixed C57BL/6J x 129SvJ background	Dr. Dieter Sau (Technische Universitat Munchen, Munchen, Germany)	Schonhuber et al 2014 PMID:20023653
Nkx2-1$^{F/F}$: *Mus musculus* mixed C57BL/6J x 129SvJ background	Dr. Shioko Kimura (NCI/NIH, Bethesda, MD)	Kusakabe et al 2006 PMID:16601074
Foxa1$^{F/F}$: *Mus musculus* mixed C57BL/6J x 129SvJ background	Dr. Klaus H. Kaestner (Upenn, Philadelphia, PA)	Gao et al 2008 PMID:19141476
Foxa2$^{F/F}$: *Mus musculus* mixed C57BL/6J x 129SvJ background	Dr. Klaus H. Kaestner (Upenn, Philadelphia, PA)	Sund et al 2000 PMID:10866673
NOD/SCID-gamma chain deficient *Mus musculus*	The Jackson Laboratory	Cat#5557

REAGENT or RESOURCE	SOURCE	IDENTIFIER
Oligonucleotides		
See STAR Methods		
Recombinant DNA		
d8.9 (plasmid)	Dr. Tyler Jacks (MIT, Cambridge, MA)	DuPage et al, 2009 PMID:19561589
VSV-G (plasmid)	Dr. Tyler Jacks (MIT, Cambridge, MA)	DuPage et al, 2009 PMID:19561589
pLKO.shNKX2-1	Addgene	Plasmid #32400
pLKO.shScramble	Addgene	Plasmid #1864
pCDH-EFS-FlpO	This Paper	N.A.
Software and algorithms		
Prism 9.0.1	GraphPad Software, LLC	9.0.1
NIS-Elements 4.30.02	Nikon	4.30.02
Analyze 12.0	Analyze Direct	12.0
Image Studio Ver 2.0	Licor	2.0
Incucyte Zoom 2016B	Essen Bioscience	2016B
Gen5 3.11.19	BioTek	3.11.19
BioRad CFX Maestro 1.1	Bio Rad	1.1
IGV 2.12.3	Broad Institute	2.12.3
GSEA 4.2.3	MSigDB	4.2.3
Adobe Illustrator 25.0	Adobe	25.0
Adobe Photoshop 22.0.1	Adobe	22.0.1
Ensembl	https://uswest.ensembl.org/index.html	Release 102
STAR	https://github.com/alexdobin/STAR	Version 2.7.6a
Clumpify	http://sourceforge.net/projects/bbmap/	Version 38.34
DEseq2	https://bioconductor.org/packages/release/bioc/html/DESeq2.html	Version 1.34.0
10X cellranger mkfastq	10x Genomics	Version 3.1.0
10X Genomics' Cell Loupe Browser	10X Genomics	Version 5.0
IlluminaBCL2 Fastq	https://support.illumina.com/sequencing/sequencing_software/bcl2fastq-conversion-software.html	N.A.
Novocraft novoalign	http://www.novocraft.com	Version 4.03.01
samtools	https://github.com/samtools/samtools	Version 1.10 DOI: 10.1093/bioinformatics/btp352
MultiRepMacsChIPSeq	https://github.com/HuntsmanCancerInstitute/MultiRepMacsChIPSeq	Version 17
MACS2	https://github.com/macs3-project/MACS	Version 2.2.6 DOI: 10.1186/gb-2008-9-9-r137
BEDtools	https://github.com/arq5x/bedtools2	Version 2.28.0 DOI: 10.1093/bioinformatics/btq033

REAGENT or RESOURCE	SOURCE	IDENTIFIER
BioToolBox	https://github.com/tjparnell/biotoolbox	Version 1.68
MAnorm2	https://github.com/tushiqi/MAnorm2	DOI: 10.1101/gr.262675.120
pHeatmap	https://CRAN.Rproject.org/package=pheatmap	N.A.
ggpiot2	https://ggplot2.tidyverse.org/	N.A.
ChIPseeker	https://bioconductor.org/packages/release/bioc/html/ChIPseeker.html	N.A.